Manifold-aware Representation Learning for Degradation-agnostic Image Restoration

Bin Ren[1,2,3] **Yawei Li**[4] **Xu Zheng**[3,5] **Yuqian Fu**[3]
Danda Pani Paudel[3] **Ming-Hsuan Yang**[6] **Luc Van Gool**[3] **Nicu Sebe**[2]
[1]University of Pisa [2]University of Trento [3]INSAIT, Sofia University “St. Kliment Ohridski” [4]ETH Zürich
[5]Hong Kong University of Science and Technology (Guangzhou) [6]University of California, Merced

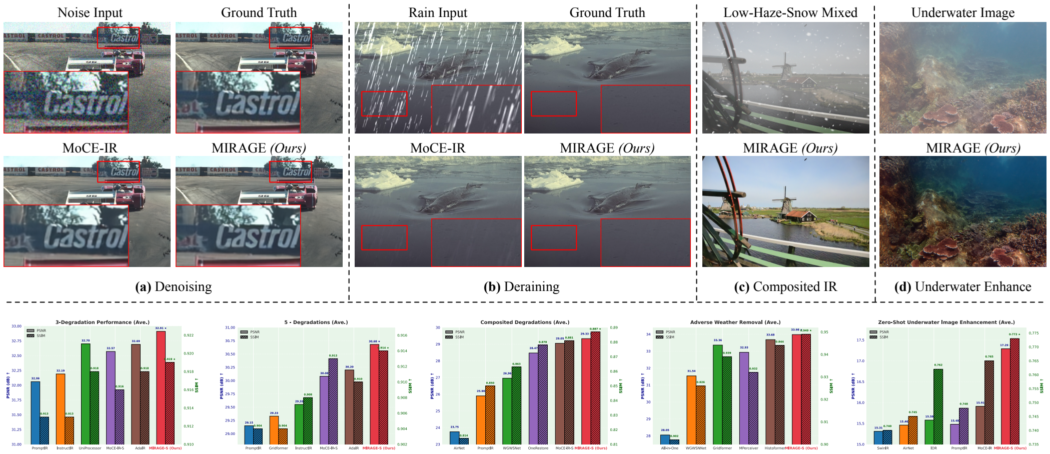

(a) Denoising **(b)** Deraining **(c)** Composited IR **(d)** Underwater Enhance

(e) Average (Ave.) Performance Comparison for: ***3 Degradation***, ***5 Degradation***, ***Composited Degradation***, ***Adverse Weather Removal***, and ***Zero-Shot Underwater Image Enhancement.***

Figure 1: *(a)-(d)*: Visual comparison for Denoising, Deraining, Composited Degradations (low-light, haze, and snow), and underwater image enhancement. *(e)*: The average PSNR and SSIM comparison across 4 challenging all-in-one and 1 zero-shot settings (Please zoom in for a better view).

Abstract

Image Restoration (IR) aims to recover high-quality images from degraded inputs affected by various corruptions such as noise, blur, haze, rain, and low-light conditions. Despite recent advances, most existing approaches treat IR as a direct mapping problem, relying on shared representations across degradation types without modeling their structural diversity. In this work, we present MIRAGE, a unified and lightweight framework for all-in-one IR that explicitly decomposes the input feature space into three semantically aligned parallel branches, each processed by a specialized module—attention for global context, convolution for local textures, and MLP for channel-wise statistics. This modular decomposition significantly improves generalization and efficiency across diverse degradations. Furthermore, we introduce a cross-layer contrastive learning scheme that aligns shallow and latent features to enhance the discriminability of shared representations. To better capture the underlying geometry of feature representations, we perform contrastive learning in a Symmetric Positive Definite (SPD) manifold space rather than the conventional Euclidean space. Extensive experiments show that MIRAGE not only achieves new state-of-the-art performance across a variety of degradation types but also offers a scalable solution for real-world IR scenarios. Our code and models will be publicly available at our Project Page.

Preprint. Under review.

1 Introduction

Image Restoration (IR) is a fundamental yet challenging problem in computer vision, aiming to reconstruct clean images from their degraded versions affected by a variety of real-world corruptions, including noise, blur, haze, rain, low-light conditions, and more [95, 41, 64, 93, 53, 60]. While recent advances have made great strides by designing powerful architectures based on Convolutional Neural Networks (CNNs), Multi-Layer Perceptrons (MLPs), and Transformers [17, 64, 107], most existing methods view restoration as a direct mapping problem—learning a global function that transforms the corrupted input into its clean counterpart. These approaches typically rely on shared representations across all degradation types, often overlooking the structural distinctions among them. As a result, they struggle to generalize when confronted with unseen or mixed degradations.

In reality, different degradation types, such as noise, haze, rain, snow, and motion blur, arise from fundamentally different physical processes and can be roughly categorized as additive, multiplicative, or kernel-based corruptions. Simultaneously, basic architectural modules exhibit distinct processing biases: convolutional filters excel at modeling local texture, attention mechanisms capture global dependencies, and MLPs often enhance channel-wise statistics. This leads to a key insight: *To handle diverse and complex degradations effectively, a restoration model should be equipped with multiple processing capabilities.* However, designing such a unified framework is non-trivial. A naive combination of CNNs, MLPs, and attention units often leads to redundancy, optimization difficulty, and computational inefficiency. In this work, we revisit the widely observed redundancy in attention mechanisms, particularly along the channel dimension [76, 27, 15]. This phenomenon has been extensively validated in both the natural language processing (NLP) and vision communities, showing that many attention heads or channels contribute minimally to performance. Rather than avoiding this redundancy, we propose to exploit it to build an efficient, modular, and generalizable architecture. We present MIRAGE, a unified and lightweight IR framework that explicitly decomposes feature processing into three semantically aligned branches. Specifically, we split the input feature map along the channel dimension and assign each partition to a specialized module: attention for global context modeling, convolution for local texture enhancement, and MLP for channel-wise refinement. This structured decomposition not only enhances expressiveness but also reduces computational complexity, yielding a powerful backbone that performs competitively across a wide range of degradation scenarios.

While MIRAGE already provides strong results and surpasses many state-of-the-art methods, we observe that its performance primarily stems from its architectural expressiveness rather than an explicit understanding of degradation-specific semantics. Motivated by recent efforts such as AirNet and PromptIR, which incorporate degradation cues into the learning process, we argue that *degradation-guided processing can make the shared representation more discriminative and significantly improve generalization across diverse restoration tasks*. To this end, we introduce a novel cross-layer contrastive learning strategy. Unlike conventional contrastive learning, which relies on complex augmentations, heavy architectures, or multi-stage training, we take a simple yet effective approach. Inspired by deeply supervised networks [33], we hypothesize that natural contrastive pairs exist within the model itself, *i.e.*, between shallow and deeper latent representations. These layers carry complementary characteristics: shallow features are rich in spatial details and noise sensitivity, while latent features are more abstract and semantically consistent. Aligning them can improve both robustness and generalization. Furthermore, instead of applying contrastive loss in Euclidean space, which can misrepresent feature similarity, we perform it in the Symmetric Positive Definite (SPD) manifold space, leading to more meaningful geometric alignment.

Inspired by the metaphor of uncovering the latent clean scene beneath complex degradations, just as a mirage reveals a hidden reality, our method learns a degradation-agnostic representation by dynamically balancing global context, local structure, and channel-wise distribution. This synergy between architectural modularity and contrastive regularization makes MIRAGE a powerful and general-purpose backbone for challenging all-in-one image restoration.

Our main contributions are as follows:

- We propose MIRAGE, a lightweight and unified IR framework that synergistically integrates attention, convolution, and MLP through structured channel-wise decomposition, enabling robust performance across diverse degradation types.

- We introduce a simple yet effective cross-layer contrastive learning strategy that aligns shallow and latent features within the SPD manifold space, thereby enhancing feature discriminability and generalization. Our approach respects the intrinsic geometry of deep representations and improves restoration quality, all without relying on data augmentation or multi-stage training.
- Extensive experiments across diverse restoration tasks demonstrate the effectiveness and efficiency of our approach. We hope MIRAGE can serve as a strong and practical baseline to inspire future research in all-in-one image restoration.

2 Related Work

Image Restoration (IR) with Various Basic Architectures. IR aims to address a highly ill-posed problem: reconstructing high-quality images from their degraded versions. Given its broad importance, IR has been widely applied in numerous applications [70, 86, 3, 42, 94]. Early IR methods primarily relied on model-based solutions that searched for closed-form solutions to predefined formulations. With the advent of deep neural networks, learning-based approaches have rapidly gained popularity. A wide range of methods have emerged, including regression-based techniques [45, 32, 44, 8, 41, 103] and generative model-based pipelines [22, 80, 50, 92, 105], built upon convolutional [14, 101, 100, 79], MLP-based [73], state space models [24, 108, 23, 12], and Vision Transformer (ViT)-based architectures [44, 65, 41, 95, 17, 46]. Despite the impressive performance of recent state-of-the-art methods, most IR solutions are still designed to address specific degradation types, such as denoising [101, 104], dehazing [69, 84], deraining [29, 66], deblurring [31, 67], and others.

Degradation-agnostic Image Restoration. While training task-specific models to handle individual types of degradation can be effective, it poses practical limitations due to the need for separate models for each degradation. In real-world scenarios, images often suffer from a mixture of degradations and artifacts, making it difficult to address each type independently. Task-specific solutions also demand considerable computational and storage resources, significantly increasing their environmental footprint. To overcome these limitations, the emerging field of All-in-One image restoration focuses on single-blind models capable of handling multiple degradation types simultaneously [93, 97, 106]. For example, AirNet [36] achieves blind All-in-One image restoration by using contrastive learning to derive degradation representations from corrupted images, which are then leveraged to reconstruct clean images. Building on this, IDR [99] tackles the problem by decomposing degradations into fundamental physical components and applying a two-stage meta-learning strategy. More recently, the prompt-based paradigm [60, 77, 43] has introduced a visual prompt learning module, enabling a single model to better handle diverse degradation types by leveraging the discriminative capacity of learned visual prompts. Extending this idea, some works further model prompts from a frequency perspective [11] or propose more complex architectures with additional datasets [19]. However, visual prompt modules often result in increased training time and decreased efficiency [11]. In contrast, our work aims to improve the model's ability to capture representative degradation cues without relying on heavy or complex prompt designs. Our goal is to develop an All-in-One image restorer that remains both computationally efficient and environmentally sustainable.

3 Preliminary: Degradation-Aware Architectures for Image Restoration

Image Degradation and Restoration. Image restoration aims to recover a clean image $\mathbf{x}$ from a degraded observation $\mathbf{y}$, commonly modeled as:

$$\mathbf{y} = \mathcal{D}(\mathbf{x}) + \mathbf{n}, \tag{1}$$

where $\mathcal{D}(\cdot)$ is a degradation operator and $\mathbf{n}$ is noise. Real-world degradations are diverse in nature—ranging from additive (*e.g.*, Gaussian noise, rain: $\mathbf{y} = \mathbf{x} + \mathbf{n}$), multiplicative (*e.g.*, haze, speckle: $\mathbf{y} = \mathbf{x} \cdot \mathbf{m}$), to convolutional degradations (*e.g.*, blur, super-resolution: $\mathbf{y} = \mathbf{k} * \mathbf{x} + \mathbf{n}$).

Such degradations are often entangled and spatially variant, forming compound pipelines:

$$\mathbf{y} = \mathcal{D}_3\big(\mathcal{D}_2(\mathcal{D}_1(\mathbf{x}))\big) + \mathbf{n}, \tag{2}$$

where each $\mathcal{D}_i$ captures a distinct degradation type. Addressing this diversity requires models capable of both local detail preservation and global structural reasoning.

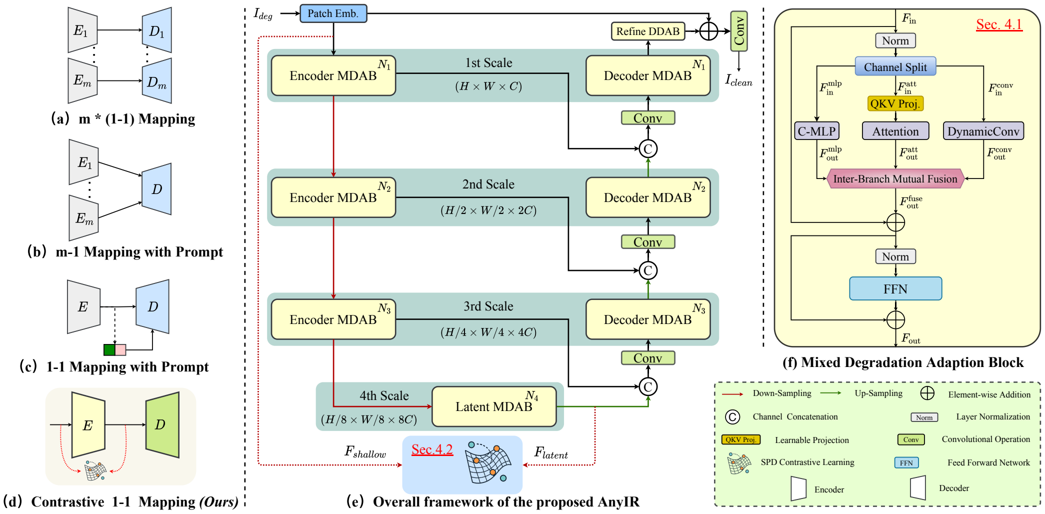

Figure 2: *(a)-(c)*: The most adopted all-in-one image restoration encodedr-decoder pipelines. *(d)*: The toy illustration of our SPD contrastive pipeline. *(e)*: The overall framework of the proposed MIRAGE : *i.e.*, a convolutional patch embedding, a U-shape encoder-decoder main body, an extra refined block, and the proposed SPD contrastive learning algorithm. *(f)*: Structure of each mixed degradation adaptation block (MDAB).

Architectural Biases for Degradation Modeling. To this end, modern deep networks adopt different inductive biases: *CNNs* capture local spatial patterns through convolution: $\mathbf{y}_p = \sum_{i \in \mathcal{N}(p)} w_i \cdot \mathbf{x}_i$. Their locality makes them effective for uniform or spatially invariant degradations. *Transformers* exploit global self-attention: $\mathbf{y}_i = \sum_j \alpha_{ij} \cdot \mathbf{V}_j$, enabling modeling of non-uniform, structured degradations such as haze or patterned noise. *MLPs*, especially token-mixing variants, use position-wise transformations: $\mathbf{y} = \mathbf{W}_2 \cdot \phi(\mathbf{W}_1 \cdot \mathbf{x})$, offering flexibility with weak spatial priors.

Each paradigm exhibits strengths and limitations in handling different degradation types. CNNs excel in local fidelity, Transformers in global context, and MLPs offer flexible feature interactions but lack inherent spatial priors. When applied to vision tasks, they often require large parameter counts and are less effective alone for structured degradations. These complementary traits motivate unified architectures that integrate them for robust, degradation-aware restoration in the wild.

4 The Proposed MIRAGE

Overview. Unlike previous methods that adopt a one-to-one mapping strategy for multiple degradations as illustrated in Fig. 2(a), which requires training a separate model for each type of degradation, our approach is more unified. Also, unlike architectures that use multiple encoders mapping to a single decoder, as shown in Fig. 2(b), which significantly increases the model size and complexity, we pursue a more efficient design. Moreover, in contrast to prompt-based methods that rely on large-scale models or introduce visual/textual prompts (Fig. 2(c)), we propose a simple yet effective mixed-backbone architecture (Fig. 2(d)). This backbone serves as a strong restoration model (Sec. 4.1), and its performance is further enhanced through cross-layer contrastive learning in the SPD space between shallow and latent features (Sec. 4.2).

4.1 Mixed Degradation Adaptation Block for AnyIR

Redundancy in MHAs Opens Opportunities for Hybrid Architectures. Redundancy has long been recognized as a fundamental limitation in multi-head self-attention (MHA), the core building block of Transformers, in both NLP and vision domains [58, 57, 85, 4, 78, 76]. Prior studies have shown that not all attention heads contribute equally, *i.e.*, some are specialized and crucial, while others can be pruned with negligible impact. This inherently implies redundancy in the channel dimension, as MHA outputs are concatenated along this axis. To empirically verify this redundancy in the context of image restoration (IR), we analyze intermediate features from a lightweight attention-only model (details in the Appendix).

Algorithm 1 Mixed Parallel Degradation Adaptation

```
Require: $F_{\text{in}}^{\text{att}}$, $F_{\text{in}}^{\text{conv}}$, $F_{\text{in}}^{\text{mlp}}$    ▷ Input features from three branches
Ensure: $F_{\text{out}}$    ▷ Final fused output
    [Att] Attention Path
 1: $Q, K, V \leftarrow \text{Linear}(F_{\text{in}}^{\text{att}})$    ▷ Projection to attention tokens
 2: $F_{\text{out}}^{\text{att}} \leftarrow \texttt{Softmax}(\frac{QK^{\top}}{\sqrt{d}})V$    ▷ Multi-head self-attention
    [Conv] Dynamic Convolution Path
 3: $F' \leftarrow \text{Conv1x1}(\text{Norm}(F_{\text{in}}^{\text{conv}}))$    ▷ Normalization and expansion
 4: $\gamma, \beta, \alpha \leftarrow \text{Split}(F')$    ▷ Gating, intermediate, convolutional paths
 5: $\alpha' \leftarrow \text{DynamicDepthwiseConv}(\alpha)$    ▷ Content-adaptive depthwise conv
 6: $\hat{F} \leftarrow \sigma(\gamma/\tau) \cdot \text{Concat}(\beta, \alpha')$    ▷ Gated local enhancement
 7: $F_{\text{out}}^{\text{conv}} \leftarrow \text{Conv1x1}(\hat{F}) + F_{\text{in}}^{\text{conv}}$    ▷ Residual projection
    [MLP] MLP Path
 8: $F_{\text{out}}^{\text{mlp}} \leftarrow \text{MLP}(F_{\text{in}}^{\text{mlp}})$    ▷ Channel-wise transformation brings more non-linearity
    [Fusion] Inter-Branch Mutual Fusion
 9: $F_{\text{out}}^{\text{att}'} \leftarrow F_{\text{out}}^{\text{att}} + \lambda_{\text{att}} \cdot \sigma(F_{\text{out}}^{\text{conv}} + F_{\text{out}}^{\text{mlp}})$    ▷ Fuse conv and MLP into attention
10: $F_{\text{out}}^{\text{conv}'} \leftarrow F_{\text{out}}^{\text{conv}} + \lambda_{\text{conv}} \cdot \sigma(F_{\text{out}}^{\text{att}} + F_{\text{out}}^{\text{mlp}})$    ▷ Fuse attention and MLP into conv
11: $F_{\text{out}}^{\text{mlp}'} \leftarrow F_{\text{out}}^{\text{mlp}} + \lambda_{\text{mlp}} \cdot \sigma(F_{\text{out}}^{\text{att}} + F_{\text{out}}^{\text{conv}})$    ▷ Fuse attention and conv into MLP
    Output Projection
12: $F_{\text{out}}^{\text{fuse}} \leftarrow \text{Project}(\text{Concat}(F_{\text{out}}^{\text{att}'}, F_{\text{out}}^{\text{conv}'}, F_{\text{out}}^{\text{mlp}'}))$    ▷ Final unified representation
13: return $F_{\text{out}}^{\text{fuse}}$
```

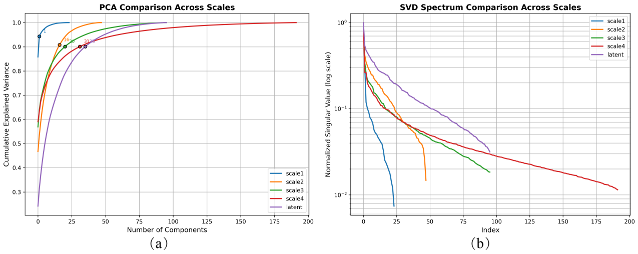

(a) (b)

Figure 3: Channel redundancy analysis across multiple feature scales. (a) Cumulative explained variance curves from PCA applied to the channel dimension of features from 1-4 scales and one latent scale. (b) Normalized singular value spectra (in log scale) of the same features via SVD. Latent feature in both plots means the channel-wise projected 4th Scale feature.

Specifically, we compute the cumulative explained variance via PCA and the normalized singular value spectra via SVD across multiple feature scales, as shown in Fig.3. As illustrated in Fig. 3(a), earlier scales (*e.g.*, 1st Scale) require significantly fewer principal components to retain most of the variance, suggesting high redundancy. Fig. 3(b) further supports this observation, with a sharper singular value decay at shallower stages, indicating stronger low-rank structure in channel-wise representations. Even at the deepest stage (*e.g.*, 4th Scale), achieving 90% variance only requires 28 out of 192 components ($\approx$ 19%), confirming that redundancy persists throughout.

This insight motivates a departure from traditional head/channel pruning. Instead of discarding redundant capacity, we propose to repurpose it by splitting the channel dimension into three parts and feeding them into distinct architectural branches, *e.g.*, attention, convolution, and MLP. This hybrid formulation leverages complementary inductive biases and makes full use of available representational space, offering a principled and efficient alternative to the previous pure MSA-based designs.

Parallel Design Brings More Efficiency. The preceding redundancy analysis reveals that many channels across scales encode overlapping information. Rather than discarding this capacity via pruning, we strategically re-purpose it through a structurally parallel design. As illustrated in Fig. 2(f), the input feature $F_{\text{in}} \in \mathbb{R}^{h \times w \times c}$ is evenly divided along the channel dimension into three sub-tensors: $F_{\text{in}}^{\text{att}}$, $F_{\text{in}}^{\text{conv}}$, and $F_{\text{in}}^{\text{mlp}}$, corresponding to attention, convolution, and MLP branches. Each branch independently processes its input using lightweight modules that specialize in distinct inductive biases, *i.e.*, global dependency modeling, local pattern extraction, and channel-wise transformation. This design reduces computation (each operation handles only a fraction of the channels) while enhancing representational diversity through architectural heterogeneity (see Lines 1-8 Alg. 1).

Inter-Branch Mutual Fusion Injects Expressivity Before FFN. While the parallel design improves efficiency and modularity, it inevitably reduces interaction across branches. To mitigate this, Lines

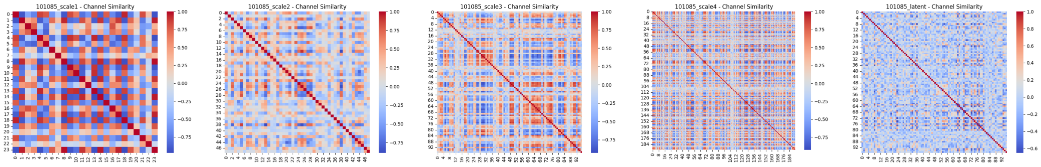

(a) (b) (c) (d) (e)

Figure 4: *(a)-(d)*: The channel-wise similarity matrix from the 1st Scale ($H \times W \times C$) to the 4th Scale ($^{H}/_{8} \times {}^{W}/_{8} \times 8C$). *(e)*: The channel-wise similarity matrix of (d) after channel-wise projection.

9–13 of Alg. 1 introduce an inter-branch mutual fusion mechanism, where each branch is enhanced via gated aggregation of the other two, modulated by learnable coefficients λ. This introduces non-linearity and cross-path context blending, reinforcing feature complementarity before unification. The fused representation is more expressive, forming a compact and effective pre-FFN encoder.

Compared to standard attention-only models where $F_{\text{out}}^{\text{att}}$ is essentially a linear combination modulated by Softmax weights, the fused output in Alg. 1 introduces richer non-linear interactions. This enhances the model's ability to fit complex degradation mappings, making it more suitable for real-world scenarios with mixed or ambiguous degradations. Subsequently, layer normalization, a feed-forward network (FFN), and a residual connection are applied: $F_{\text{out}} = \text{FFN}(\text{Norm}(F_{\text{out}}^{\text{fuse}})) + F_{\text{out}}^{\text{fuse}}$. This sequence stabilizes feature distributions and further boosts expressiveness.

4.2 Shallow-Latent Contrastive Learning via SPD Manifold Alignment

Shallow-Latent Feature Pairs are Naturally Contrastive Pairs. Features extracted at different depths exhibit fundamentally different statistical properties. As shown in Fig. 4, shallow-stage features (*e.g.*, Scale1) present sparse and decorrelated channel distributions, while deeper layers (*e.g.*, Scale4) become increasingly redundant and concentrated. This trend is quantitatively supported by the effective rank ratio across scales, which increases from only 4.2% ($^{1}/_{24}$ at 1st Scale) to 16.1% ($^{31}/_{192}$ at 4th Scale). However, by compressing the deep features through a lightweight MLP, we obtain a latent representation with a significantly higher rank ratio of 36.5% ($^{35}/_{96}$), indicating a more decorrelated and expressive embedding. This structural disparity between sparse, localized shallow features and compressed, semantic latent ones naturally defines a contrastive pairing without requiring additional augmentation. We leverage this depth-asymmetric contrast to impose consistency across stages, enabling better semantic alignment and stronger representational generalization under complex degradation conditions. *Note that this case study is conducted under noise degradation; however, similar trends are consistently observed for other degradations as well.* Please refer to our Supplementary Materials (*i.e.*, *Supp. Mat.*) for more details.

SPD Manifold Space Contrastive Learning Leads to More Discriminative Representations. To enhance representation consistency across depth, we introduce a contrastive objective defined over SPD (Symmetric Positive Definite) manifold features. Given shallow features $F_{\text{shallow}} \in \mathbb{R}^{C_s \times H \times W}$ and latent features $F_{\text{latent}} \in \mathbb{R}^{C_l \times H' \times W'}$, we first reduce their channel dimensions via 1×1 convolutions. The resulting tensors are reshaped into feature matrices $X_s, X_l \in \mathbb{R}^{C \times N}$ with $N = H \times W$, and their second-order statistics are computed as:

$$\mathbf{C}_s = \frac{1}{N-1}(X_s - \mu_s)(X_s - \mu_s)^\top + \epsilon\mathbf{I}, \quad \mathbf{C}_l = \frac{1}{N'-1}(X_l - \mu_l)(X_l - \mu_l)^\top + \epsilon\mathbf{I}, \tag{3}$$

where μ is the mean across spatial dimensions, and $\epsilon\mathbf{I}$ ensures numerical stability and positive definiteness. The SPD matrices $\mathbf{C}_s, \mathbf{C}_l \in \mathbb{R}^{C \times C}$ are vectorized and projected to a contrastive embedding space via shallow MLPs:

$$z_s = \text{Norm}(W_s \cdot \text{vec}(\mathbf{C}_s)), \quad z_l = \text{Norm}(W_l \cdot \text{vec}(\mathbf{C}_l)), \tag{4}$$

where W_s, W_l are learnable projection layers, and $\text{Norm}(\cdot)$ denotes ℓ_2-normalization. We then apply an InfoNCE-style contrastive loss to align the shallow and latent embeddings:

$$\mathcal{L}_{\text{SPD}} = -\log \frac{\exp\left(\text{sim}(z_s, z_l)/\tau\right)}{\sum_{z_l'} \exp\left(\text{sim}(z_s, z_l')/\tau\right)}, \tag{5}$$

where $\text{sim}(\cdot, \cdot)$ denotes cosine similarity, and τ is a temperature parameter. Unlike conventional Euclidean contrastive learning which treats feature vectors as flat points our SPD-based method

Table 1: *Comparison to state-of-the-art on three degradations.* PSNR (dB, ↑) and SSIM (↑) metrics are reported on the full RGB images. **Best** performances is highlighted. '-' means unreported results.

Method	Venue.	Params.	*Dehazing*		*Deraining*		*Denoising*						Average	
			SOTS		Rain100L		BSD68$_{\sigma=15}$		BSD68$_{\sigma=25}$		BSD68$_{\sigma=50}$			
BRDNet [72]	Neural Networks'22	-	23.23	.895	27.42	.895	32.26	.898	29.76	.836	26.34	.693	27.80	.843
LPNet [21]	CVPR'19	-	20.84	.828	24.88	.784	26.47	.778	24.77	.748	21.26	.552	23.64	.738
FDGAN [16]	AAAI'20	-	24.71	.929	29.89	.933	30.25	.910	28.81	.868	26.43	.776	28.02	.883
DL [20]	TPAMI'19	2M	26.92	.931	32.62	.931	33.05	.914	30.41	.861	26.90	.740	29.98	.876
MPRNet [96]	CVPR'21	16M	25.28	.955	33.57	.954	33.54	.927	30.89	.880	27.56	.779	30.17	.899
AirNet [36]	CVPR'22	9M	27.94	.962	34.90	.967	33.92	.933	31.26	.888	28.00	.797	31.20	.910
NDR [88]	TIP'24	28M	25.01	.860	28.62	.848	28.72	.826	27.88	.798	26.18	.720	25.01	.810
PromptIR [60]	NeurIPS'23	36M	30.58	.974	36.37	.972	33.98	.933	31.31	.888	28.06	.799	32.06	.913
MoCE-IR-S [93]	CVPR'25	11M	30.98	.979	38.22	.983	34.08	.933	31.42	.888	28.16	.798	32.57	.916
AdaIR [11]	ICLR'25	29M	31.06	.980	38.64	.983	34.12	.935	31.45	.892	28.19	.802	32.69	.918
MoCE-IR [93]	CVPR'25	25M	31.34	.979	38.57	.984	34.11	.932	31.45	.888	28.18	.800	32.73	.917
MIRAGE -T (*Ours*)	2025	6M	31.81	**.982**	38.44	.983	34.05	.935	31.40	**.892**	28.14	.802	32.77	.919
MIRAGE -S (*Ours*)	2025	10M	**31.86**	.981	**38.94**	**.985**	**34.12**	**.935**	**31.46**	.891	**28.19**	**.803**	**32.91**	**.919**
Methods with the assistance of vision language, multi-task learning, natural language prompts, or multi-modal control														
DA-CLIP [51]	ICLR'24	125M	29.46	.963	36.28	.968	30.02	.821	24.86	.585	22.29	.476	-	-
Art$_{PromptIR}$ [83]	ACM MM'24	36M	30.83	.979	37.94	.982	34.06	.934	31.42	.891	28.14	.801	32.49	.917
InstructIR-3D [10]	ECCV'24	16M	30.22	.959	37.98	.978	34.15	.933	31.52	.890	28.30	.804	32.43	.913
UniProcessor [18]	ECCV'24	1002M	31.66	.979	38.17	.982	34.08	.935	31.42	.891	28.17	.803	32.70	.918
VLU-Net [97]	CVPR'25	35M	30.71	.980	38.93	.984	34.13	.935	31.48	.892	28.23	.804	32.70	.919

preserves second-order channel dependencies, enabling richer structural supervision. This manifold-aware regularization aligns local and semantic features across depth, *enhances discriminability*, and *introduces no additional inference cost*.

5 Experiments

We conduct experiments adhering to the protocols of prior general image restoration works [60, 99] under four settings: *(i) All-in-One (3Degradations)*, *(ii) All-in-One (5Degradations)*, *(iii) Mixed Degradation Setting*, *(iv) Adverse Weather Removal Setting*, and *(v) Zero-Shot Setting*. More experimental details and the dataset introduction are provided in our *Supp. Mat.*

5.1 SOTA Comparison.

3 Degradations. We evaluate our all-in-one restorer, MIRAGE , against other specialized methods listed in Tab. 1, all trained on three degradations: dehazing, deraining, and denoising. MIRAGE consistently outperforms all the comparison methods, even for those with the assistance of language, multi-task, or prompts. Notably, even our 6M tiny model outperforms the baseline method PromptIR [60] by **0.71dB** on average. And the 10M small model achieves the best performance across all the metrics, while maintaining **60%** fewer parameters compared to MoCE-IR [93].

5 Degradations. Extending the three degradation tasks to include deblurring and low-light enhancement [36, 99], we validate our method's comprehensive performance in an All-in-One setting. As shown in Tab. 2, MIRAGE -S effectively leverages degradation-specific features, surpassing PromptIR [60], MoCE-IR-S [93], AdaIR [11], and VLU-Net [97] by an average of 1.53dB, 0.6dB, 0.48dB, and 0.57dB with lower parameters. Notably, our tiny model (6M) also achieves competitive results (a second-best average PSNR) compared to the MoCE-IR (25M) and outperforms all other comparison methods, even those with the assistance of other modalities, multi-task learning, or pretraining.

Composited Degradation Setting. To simulate more realistic restoration scenarios, we extend the setting from OneRestore [25] by including not only diverse single degradations—rain, haze, snow, low illumination—but also composite degradations where multiple types are combined within the same image. This results in a total of eleven distinct restoration settings. As shown in Tab. 3, our Tiny (6M) and Small (10M) models outperform OneRestore [25] (6M) by 0.39 dB and 0.86 dB on average, respectively. Compared to the recent state-of-the-art MoCE-IR [93] (11M), our Small model still achieves 0.28 dB higher performance while being more compact (10M vs. 11M). These results demonstrate the effectiveness of our method, especially in handling complex, mixed degradations.

Adverse Weather Removal Setting. Following [74, 110], We test our MIRAGE on three challenging deweathering tasks: snow removal, rain streak and fog removal, and raindrop removal. Tab. 4

Table 2: *Comparison to state-of-the-art on five degradations.* PSNR (dB, ↑) and SSIM (↑) metrics are reported on the full RGB images with (*) denoting general image restorers, others are specialized all-in-one approaches. **Best** performance is highlighted.

Method	Venue	Params.	*Dehazing*		*Deraining*		*Denoising*		*Deblurring*		*Low-Light*		Average	
			SOTS		Rain100L		BSD68$_{\sigma=25}$		GoPro		LOLv1			
NAFNet* [6]	ECCV'22	17M	25.23	.939	35.56	.967	31.02	.883	26.53	.808	20.49	.809	27.76	.881
DGUNet* [55]	CVPR'22	17M	24.78	.940	36.62	.971	31.10	.883	27.25	.837	21.87	.823	28.32	.891
SwinIR* [44]	ICCVW'21	1M	21.50	.891	30.78	.923	30.59	.868	24.52	.773	17.81	.723	25.04	.835
Restormer* [95]	CVPR'22	26M	24.09	.927	34.81	.962	31.49	.884	27.22	.829	20.41	.806	27.60	.881
MambaIR* [24]	ECCV'24	27M	25.81	.944	36.55	.971	31.41	.884	28.61	.875	22.49	.832	28.97	.901
DL [20]	TPAMI'19	2M	20.54	.826	21.96	.762	23.09	.745	19.86	.672	19.83	.712	21.05	.743
Transweather [74]	CVPR'22	38M	21.32	.885	29.43	.905	29.00	.841	25.12	.757	21.21	.792	25.22	.836
TAPE [47]	ECCV'22	1M	22.16	.861	29.67	.904	30.18	.855	24.47	.763	18.97	.621	25.09	.801
AirNet [36]	CVPR'22	9M	21.04	.884	32.98	.951	30.91	.882	24.35	.781	18.18	.735	25.49	.847
IDR [99]	CVPR'23	15M	25.24	.943	35.63	.965	31.60	.887	27.87	.846	21.34	.826	28.34	.893
PromptIR [60]	NeurIPS'23	36M	26.54	.949	36.37	.970	31.47	.886	28.71	.881	22.68	.832	29.15	.904
MoCE-IR-S [93]	CVPR'25	11M	31.33	.978	37.21	.978	31.25	.884	28.90	.877	21.68	.851	30.08	.913
AdaIR [11]	ICLR'25	29	30.53	.978	38.02	.981	31.35	.889	28.12	.858	23.00	.845	30.20	.910
MoCE-IR [93]	CVPR'25	25M	30.48	.974	38.04	.982	31.34	.887	**30.05**	**.899**	23.00	.852	30.58	**.919**
MIRAGE -T *(Ours)*	2025	6M	31.35	.979	38.24	.983	31.35	.891	27.98	.850	23.11	.854	30.41	.912
MIRAGE -S *(Ours)*	2025	10M	**31.45**	**.980**	**38.92**	**.985**	**31.41**	**.892**	28.10	.858	**23.59**	**.858**	**30.68**	.914
Methods with the assistance of natural language prompts or multi-task learning														
InstructIR-5D [10]	ECCV'24	16M	36.84	.973	27.10	.956	31.40	.887	29.40	.886	23.00	.836	29.55	.908
Art$_{PromptIR}$ [83]	ACM MM'24	36M	29.93	.908	22.09	.891	29.43	.843	25.61	.776	21.99	.811	25.81	.846
VLU-Net [97]	CVPR'25	35M	30.84	.980	38.54	.982	31.43	.891	27.46	.840	22.29	.833	30.11	.905

Table 3: *Comparison to state-of-the-art on composited degradations.* PSNR (dB, ↑) and SSIM (↑) are reported on the full RGB images. Our method consistently outperforms even larger models, with favorable results in composited degradation scenarios.

Method	Params.	*CDD11-Single*								*CDD11-Double*										*CDD11-Triple*				Avg.	
		Low (L)		Haze (H)		Rain (R)		Snow (S)		L+H		L+R		L+S		H+R		H+S		L+H+R		L+H+S			
AirNet [36]	9M	24.83	.778	24.21	.951	26.55	.891	26.79	.919	23.23	.779	22.82	.710	23.29	.723	22.21	.868	23.29	.901	21.80	.708	22.24	.725	23.75	.814
PromptIR [60]	36M	26.32	.805	26.10	.969	31.56	.946	31.53	.960	24.49	.789	25.05	.771	24.51	.761	24.54	.924	23.70	.925	23.74	.752	23.33	.747	25.90	.850
WGWSNet [109]	26M	24.39	.774	27.90	.982	33.15	.964	34.43	.973	24.27	.800	25.06	.772	24.60	.765	27.23	.955	27.65	.960	23.90	.772	23.97	.771	26.96	.863
WeatherDiff [59]	83M	23.58	.763	21.99	.904	24.85	.885	24.80	.888	21.83	.756	22.69	.730	22.12	.707	21.25	.868	21.99	.868	21.23	.716	21.04	.698	22.49	.799
OneRestore [25]	6M	26.48	.826	32.52	.990	33.40	.964	34.31	.973	25.79	.822	25.58	.799	25.19	.789	29.99	.957	30.21	.964	24.78	.788	24.90	.791	28.47	.878
MoCE-IR [93]	11M	27.26	.824	32.66	.990	34.31	.970	35.91	.980	26.24	.817	26.25	.800	26.04	.793	29.93	.964	30.19	.970	25.41	.789	25.39	.790	29.05	.881
MIRAGE (*ours*)	6M	27.13	.830	32.39	.989	34.23	.969	35.57	.978	26.04	.823	26.21	.807	26.07	.799	29.49	.962	29.72	.967	25.17	.793	25.41	.793	28.86	.883
MIRAGE (*ours*)	10M	**27.41**	**.833**	**33.12**	**.992**	**34.66**	**.971**	**35.98**	**.981**	**26.55**	**.828**	**26.53**	**.810**	**26.33**	**.803**	**30.32**	**.965**	**30.27**	**.969**	**25.59**	**.801**	**25.86**	**.799**	**29.33**	**.887**

shows the comparison of our MIRAGE and other state-of-the-art methods. MIRAGE consistently outperforms existing methods across almost all datasets except the PSNR performance for RainDrop. The significant performance gains over multiple weather degradations demonstrate the effectiveness of MIRAGE in handling diverse weather-related degradations. Especially, 0.3 dB improvement on PSNR over Histoformer [71] and 1.05 dB improvements over MPerceiver [1].

Zero-Shot Cross-Domain (*i.e.*, Underwater) Setting. We evaluate our method's generalization under a challenging zero-shot setting using real-world underwater images. As shown in Tab. 5, MIRAGE -S achieves 17.29 dB and 0.773 SSIM, surpassing the best prior method MoCE-IR [93] by a clear margin (+1.38 dB PSNR), while being more compact. Importantly, our model has never seen underwater data during training. This demonstrates that our adaptive modeling not only fits mixed degradations but also transfers robustly to unseen, conditions.

Efficiency Comparison. Tab. 6 presents a detailed comparison of PSNR, memory usage, parameter count, and FLOPs. Our Tiny model (MIRAGE -T) achieves the best efficiency-performance trade-off: with only 6.21M parameters and 16G FLOPs, it outperforms all prior methods, including larger models like PromptIR [60] and MoCE-IR-S [93]. Notably, MIRAGE -T surpasses MoCE-IR-S by +0.26 dB while requiring less than half the computational cost. Even our Small variant (MIRAGE -S) exceeds full MoCE-IR in both PSNR (+0.18 dB) and FLOPs (27G vs. 75G). These results validate that our design achieves strong restoration quality without sacrificing computational efficiency.

Visual Comparison. Across various restoration tasks, MIRAGE consistently produces sharper structures, richer textures, and fewer artifacts compared to existing methods. Fig. 1 demonstrates its strong generalization and ability to recover fine-grained details under diverse degradations, showing superior performance than others. More visual results are provided in our *Supp. Mat.*

Table 4: Comparisons for *4-task adverse weather removal*. Missing values are denoted by '–'.

Method	**Venue**	**Snow100K-S** [48]		**Snow100K-L** [48]		**Outdoor-Rain** [38]		**RainDrop** [61]		**Average**	
		PSNR	SSIM	PSNR	SSIM	PSNR	SSIM	PSNR	SSIM	PSNR	SSIM
All-in-One [40]	CVPR'20	–	–	28.33	.882	24.71	.898	31.12	.927	28.05	.902
TransWeather [75]	CVPR'22	32.51	.934	29.31	.888	28.83	.900	30.17	.916	30.20	.909
Chen *et al.* [7]	CVPR'22	34.42	.947	30.22	.907	29.27	.915	31.81	.931	31.43	.925
WGWSNet [109]	CVPR'23	34.31	.946	30.16	.901	29.32	.921	32.38	.938	31.54	.926
WeatherDiff$_{64}$ [59]	TPAMI'23	35.83	.957	30.09	.904	29.64	.931	30.71	.931	31.57	.931
WeatherDiff$_{128}$ [59]	TPAMI'23	35.02	.952	29.58	.894	29.72	.922	29.66	.923	31.00	.923
AWRCP [90]	ICCV'23	36.92	.965	31.92	.934	31.39	.933	31.93	.931	33.04	.941
GridFormer [13]	IJCV'24	37.46	.964	31.71	.923	31.87	.933	32.39	.936	33.36	.939
MPerceiver [1]	CVPR'24	36.23	.957	31.02	.916	31.25	.925	**33.21**	.929	32.93	.932
DTPM [91]	CVPR'24	37.01	.966	30.92	.917	30.99	.934	32.72	.944	32.91	.940
Histoformer [71]	ECCV'24	37.41	.966	32.16	.926	32.08	.939	33.06	.944	33.68	.944
MIRAGE -S *(Ours)*	2025	**37.97**	**.973**	**32.33**	**.929**	**32.82**	**.949**	32.78	**.945**	**33.98**	**.949**

Table 5: *Zero-Shot* Cross-Domain Underwater Image Enhancement Results.

Method	PSNR (dB, ↑)	SSIM (↑)
SwinIR [44]	15.31	.740
NAFNet [9]	15.42	.744
Restormer [95]	15.46	.745
AirNet [36]	15.46	.745
IDR [99]	15.58	.762
PromptIR [60]	15.48	.748
MoCE-IR [93]	15.91	.765
MIRAGE -S *(Ours)*	**17.29**	**.773**

Table 6: *Complexity Analysis.* FLOPs are computed on an image of size 224 × 224 using a NVIDIA Tesla A100 (40G) GPU.

Method	PSNR (dB, ↑)	Memory (↓)	Params. (↓)	FLOPs (↓)
AirNet [36]	31.20	4829M	8.93M	238G
PromptIR [60]	32.06	9830M	35.59M	132G
IDR [99]	-	4905M	15.34M	98G
AdaIR [11]	-	9740M	28.79M	124G
MoCE-IR-S [93]	32.51	4263M	11.48M	37G
MoCE-IR [93]	32.73	6654M	25.35M	75G
MIRAGE -T *(Ours)*	32.77	**3729M**	**6.21M**	**16G**
MIRAGE -S *(Ours)*	**32.91**	4810M	9.68M	27G

5.2 Ablation Study.

We conduct ablation studies to assess the contribution of key components in MIRAGE , as summarized in Tab. 7. Starting from an attention-only baseline (32.23 dB, 19.89M), we progressively integrate each module while reducing overall complexity. Removing the dynamic convolution branch (*w/o DynamicConv*) causes a 0.56 dB drop, indicating its importance for local spatial modeling. The channel-wise MLP (*w/o C-MLP*) also plays a critical role, with a 0.38 dB performance loss. Replacing gated fusion with naive concatenation (*w/o Fusion*) leads to a further 0.20 dB drop, confirming that explicit feature integration is more effective. On the regularization side, removing contrastive learning (*w/o CL & SPD*) or only the SPD module degrades performance by 0.14 dB and 0.24 dB respectively, highlighting the benefit of manifold-aware cross-depth alignment. Overall, each component contributes to the final performance. Our full model achieves the best balance between accuracy and efficiency with only 6.21M parameters and 32.77 dB PSNR.

Table 7: *Ablation Study* of MIRAGE -T on 3 Degradation Setting.

Ablaton	Parms.	Results	
		PSNR (dB, ↑)	SSIM(↓)
att-only *(Ours)*	19.89 M	32.23 (-0.54)	.912
w/o DynamicConv	9.43 M	32.21 (-0.56)	.911
w/o C-MLP	7.01 M	32.39 (-0.38)	.913
w/o Fusion (*i.e.* Cat()-Only)	5.71 M	32.57 (-0.20)	.914
w/o CL & SPD	5.80M	32.63 (-0.14)	.916
w/o SPD	6.10M	32.53 (-0.24)	.914
MIRAGE -T *(Full)*	6.21M	32.77	.919

6 Conclusion

In this paper, we present MIRAGE , a unified and lightweight framework for all-in-one image restoration. By decomposing features into attention-, convolution-, and MLP-based branches, MIRAGE captures global context, local textures, and channel-wise statistics in a complementary and efficient manner. To bridge the semantic gap across depths, we introduce a shallow-latent contrastive learning scheme that aligns early and latent representations via second-order feature statistics on the SPD manifold. This improves cross-stage consistency and enhances representation discriminability without additional inference cost. Extensive experiments across diverse degradations and cross-domain settings show that MIRAGE achieves state-of-the-art performance with minimal parameters and FLOPs. We believe its design offers a scalable path for lightweight, adaptive restoration, with potential extensions to video and multi-modal scenarios. Please refer to our *Supp. Mat.* for additional discussions, implementation details, and visual results.

A Experimental Protocols

A.1 Datasets

3 Degradation Datasets. For both the All-in-One and single-task settings, we follow the evaluation protocols established in prior works [36, 60, 93], utilizing the following datasets: For image denoising in the single-task setting, we combine the BSD400 [2] and WED [52] datasets, and corrupt the images with Gaussian noise at levels $\sigma \in \{15, 25, 50\}$. BSD400 contains 400 training images, while WED includes 4,744 images. We evaluate the denoising performance on BSD68 [54] and Urban100 [26]. For single-task deraining, we use Rain100L [87], which provides 200 clean/rainy image pairs for training and 100 pairs for testing. For single-task dehazing, we adopt the SOTS dataset [35], consisting of 72,135 training images and 500 testing images. Under the All-in-One setting, we train a unified model on the combined set of the aforementioned training datasets for 120 epochs and directly test it across all three restoration tasks.

5 Degradation Datasets. The 5-degradation setting is built upon the 3-degradation setting, with two additional tasks included: deblurring and low-light enhancement. For deblurring, we adopt the GoPro dataset [56], which contains 2,103 training images and 1,111 testing images. For low-light enhancement, we use the LOL-v1 dataset [81], consisting of 485 training images and 15 testing images. Note that for the denoising task under the 5-degradation setting, we report results using Gaussian noise with $\sigma = 25$. The training takes 130 epochs.

Composited Degradation Datasets. Regarding the composite degradation setting, we use the CDD11 dataset [25]. CDD11 consists of 1,183 training images for: *(i) 4 kinds of single-degradation types:* haze (H), low-light (L), rain (R), and snow (S); *(ii) 5 kinds of double-degradation types:* low-light + haze (l+h), low-light+rain (L+R), low-light + snow (L+S), haze + rain (H+R), and haze + snow (H+S). *(iii) 2 kinds of Triple-degradation type:* low-light + haze + rain (L+H+R), and low-light + haze + snow (L+H+S). We train our method for 150 epochs (fewer than 200 epochs than MoCE-IR [93]), and we keep all other settings unchanged.

Adverse Weather Removal Datasets. For the deweathering tasks, we follow the experimental setups used in TransWeather [75] and WGWSNet [109], evaluating the performance of our approach on multiple synthetic datasets. We assess the capability of MIRAGE across three challenging tasks: snow removal, rain streak and fog removal, and raindrop removal. The training set, referred to as "AllWeather", is composed of images from the Snow100K [49], Raindrop [62], and Outdoor-Rain [39] datasets. For testing, we evaluate our model on the following subsets: Snow100K-S (16,611 images), Snow100K-L (16,801 images), Outdoor-Rain (750 images), and Raindrop (249 images). Same as Histoformer [71], we train MIRAGE on "AllWeather" with 300,000 iterations.

Zero-Shot Underwater Image Enhancement Dataset. For the zero-shot underwater image enhancement setting, we follow the evaluation protocol of DCPT [28] by directly applying our model, trained under the 5-degradation setting, on the UIEB dataset [37] without any finetuning. UIEB consists of two subsets: 890 raw underwater images with corresponding high-quality reference images, and 60 challenging underwater images. We evaluate our zero-shot performance on the 890-image subset with available reference images.

A.2 Implementation Details

Implementation Details. Our MIRAGE framework is designed to be end-to-end trainable, removing the need for multi-stage optimization of individual components. The architecture adopts a robust 4-level encoder-decoder structure, with a varying number of Mixed Degradation Attention Blocks (MDAB) at each level—specifically $[3, 5, 5, 7]$ from highest to lowest resolution in the Tiny variant. Following prior works [60, 93], we train the model for 120 epochs with a batch size of 32 in both the 3-Degradation All-in-One and single-task settings. The optimization uses a combination of L_1 and Fourier loss, optimized with Adam [30] (initial learning rate of 2×10^{-4}, $\beta_1 = 0.9$, $\beta_2 = 0.999$) and a cosine decay schedule. During training, we apply random cropping to 128×128 patches, along with horizontal and vertical flipping as data augmentation. All experiments are conducted on a single NVIDIA H200 GPU (140 GB). Memory usage is approximately 42 GB for the Tiny (*i.e.*, MIRAGE -T) model and 56 GB for the Small model (*i.e.*, MIRAGE -S).

Model Scaling. We propose two scaled variants of our MIRAGE , namely Tiny (MIRAGE -T) and Small (MIRAGE -S). As detailed in Tab. A, these variants differ in terms of the number of MDAB

Table A: The details our the tiny and small version of our MIRAGE . FLOPs are computed on an image of size 224 × 224 using a NVIDIA Tesla A100 (40G) GPU.

	MIRAGE -T	MIRAGE -S
The Number of the MDAB crosses 4 scales	[3, 5, 5, 7]	[3, 5, 5, 7]
The Input Embedding Dimension	24	30
The FFN Expansion Factor	2	2
The Number of the Refinement Blocks	2	3
Params. (↓)	6.21M	9.68 M
FLOPs (↓)	16 G	27 G

Table B: *Comparison to state-of-the-art for single degradations.* PSNR (dB, ↑) and SSIM (↑) metrics are reported on the full RGB images. **Best** performance is highlighted. Our method excels over prior works.

(a) *Dehazing*

Method	Params.	SOTS	
DehazeNet [5]	-	22.46	.851
MSCNN [68]	-	22.06	.908
AODNet [34]	-	20.29	.877
EPDN [63]	-	22.57	.863
FDGAN [16]	-	23.15	.921
AirNet [36]	9M	23.18	.900
PromptIR [60]	36M	31.31	.973
MIRAGE (*Ours*)	**6M**	31.46	.977
MIRAGE (*Ours*)	10M	**31.53**	**.980**

(b) *Deraining*

Method	Params.	Rain100L	
DIDMDN [98]	-	23.79	.773
UMR [89]	-	32.39	.921
SIRR [82]	-	32.37	.926
MSPFN [29]	-	33.50	.948
LPNet [21]	-	23.15	.921
AirNet [36]	9M	34.90	.977
PromptIR [60]	36M	37.04	.979
MIRAGE (*ours*)	**6M**	37.47	.980
MIRAGE (*Ours*)	10M	**38.01**	**.982**

(c) *Denoising* on BSD68

Method	Params.	σ=15		σ=25		σ=50	
DnCNN [100]	-	33.89	.930	31.23	.883	27.92	.789
IRCNN [101]	-	33.87	.929	31.18	.882	27.88	.790
FFDNet [102]	-	33.87	.929	31.21	.882	27.96	.789
BRDNet [72]	-	34.10	.929	31.43	.885	28.16	.794
AirNet [36]	9M	34.14	.936	31.48	.893	28.23	.806
PromptIR [60]	36M	34.34	.938	31.71	.897	28.49	.813
PromptIR [60] (Repdoduce)	36M	34.15	.934	31.50	.894	28.33	.807
MIRAGE (*ours*)	**6M**	34.23	.936	31.60	.896	28.36	.808
MIRAGE (*Ours*)	10M	**34.25**	**.937**	**31.65**	**.898**	**28.38**	**.810**

blocks across scales, the input embedding dimension, the FFN expansion factor, and the number of refinement blocks.

A.3 Optimization Objectives

The overall optimization objective of our approach is defined as:

$$\mathcal{L}_{\text{total}} = \mathcal{L}_1 + \lambda_{fre} \times \mathcal{L}_{\text{Fourier}} + \lambda_{ctrs} \times \mathcal{L}_{\text{SPD}}. \tag{6}$$

Here, $\mathcal{L}_{\text{Fourier}}$ denotes the real-valued Fourier loss computed between the restored image and the ground-truth image, and $\mathcal{L}_{\text{SPD}}$ represents our proposed contrastive learning objective in the SPD (Symmetric Positive Definite) space.

Specifically, we adopt an ℓ_1 loss that adopted in IR tasks [60, 93, 36, 11, 64], defined as $\mathcal{L}_1 = |\hat{x} - x|_1$, to enforce pixel-wise similarity between the restored image $\hat{x}$ and the ground-truth image x. $\mathcal{L}_{\text{Fourier}}$, as utilized in MoCE-IR [93, 11], to enhance frequency-domain consistency, the real-valued Fourier loss, is defined as:

$$\mathcal{L}_{\text{Fourier}} = \|\mathcal{F}_{\text{real}}(\hat{x}) - \mathcal{F}_{\text{real}}(x)\|_1 + \|\mathcal{F}_{\text{imag}}(\hat{x}) - \mathcal{F}_{\text{imag}}(x)\|_1 , \tag{7}$$

where $\hat{x}$ and x denote the restored and ground-truth images, respectively. $\mathcal{F}_{\text{real}}(\cdot)$ and $\mathcal{F}_{\text{imag}}(\cdot)$ represent the real and imaginary parts of the 2D real-input FFT (*i.e.*, rfft2). The final loss is computed as the ℓ_1 distance between the real and imaginary components of the predicted and target frequency spectra. Same as MoCE-IR [93], λ_{fre} is set to 0.1 throughout our experiments. Meanwhile, the $\mathcal{L}_{\text{SPD}}$ is defined as in Eq. 3-5 of our main manuscript. More ablation studies regarding the proposed $\mathcal{L}_{\text{SPD}}$ are provided in Sec. B.3. The temperature parameter τ of the proposed $\mathcal{L}_{\text{SPD}}$ is set to 0.1 throughout all the experiments.

B More Method Details & Supplementary Experiments

B.1 1 Deg. Comparison

Single-Degradation. Tab. B presents the results of MIRAGE trained individually for dehazing, deraining, and denoising. Across all tasks, our method consistently surpasses previous state-of-the-art approaches, including PromptIR [60] and its reproduced variant. Particularly in the denoising task on BSD68, our model achieves the best performance across all noise levels. Interestingly, while the

Algorithm A DynamicDepthwiseConv

```
Require: $\alpha \in \mathbb{R}^{B\times C\times H\times W}$    ▷ Input feature map
Ensure: $\alpha' \in \mathbb{R}^{B\times C\times H\times W}$    ▷ Output after dynamic depthwise conv
    [Step 1] Generate Dynamic Kernel
    $K \leftarrow \texttt{AdaptiveAvgPool2D}(\alpha)$    ▷ Global context pooling
    $K \leftarrow \texttt{Conv2D}(K,\ 1\times 1,\ \text{out\_ch} = C)$    ▷ Linear projection
    $K \leftarrow \texttt{GELU}(K)$    ▷ Non-linear activation
    $K \leftarrow \texttt{Conv2D}(K,\ 1\times 1,\ \text{out\_ch} = C\cdot k^2)$    ▷ Generate kernel weights
    $K \leftarrow \texttt{Reshape}(K,\ [B\cdot C,\ 1,\ k,\ k])$    ▷ Form depthwise filters
    [Step 2] Apply Depthwise Convolution
    $\alpha_{\text{flat}} \leftarrow \texttt{Reshape}(\alpha,\ [1,\ B\cdot C,\ H,\ W])$    ▷ Prepare for grouped conv
    $\alpha'_{\text{flat}} \leftarrow \texttt{Conv2D}(\alpha_{\text{flat}},\ K,\ \text{groups} = B\cdot C,\ \text{padding} = k \div 2)$    ▷ Apply dynamic depthwise conv
    $\alpha' \leftarrow \texttt{Reshape}(\alpha'_{\text{flat}},\ [B,\ C,\ H,\ W])$    ▷ Reshape back to original shape
    return $\alpha'$
```

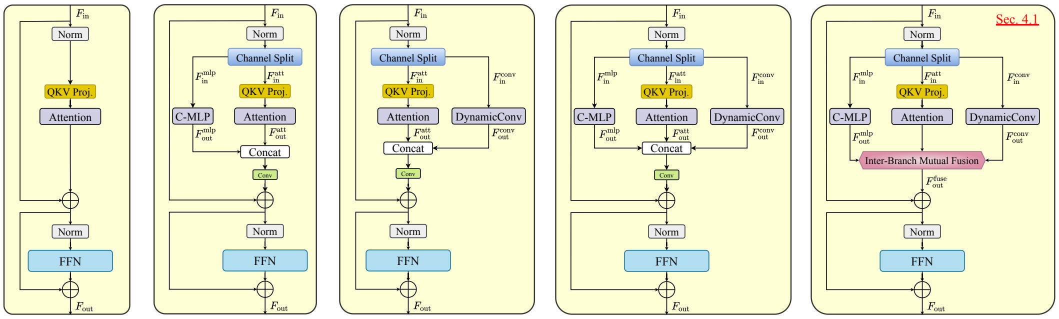
F_{in}
Norm
QKV Proj.
Attention
Norm
FFN
F_{out}
Channel Split
$F_{\text{in}}^{\text{mlp}}$
$F_{\text{in}}^{\text{att}}$
$F_{\text{in}}^{\text{conv}}$
C-MLP
DynamicConv
$F_{\text{out}}^{\text{mlp}}$
$F_{\text{out}}^{\text{att}}$
$F_{\text{out}}^{\text{conv}}$
Concat
Conv
Inter-Branch Mutual Fusion
$F_{\text{out}}^{\text{fuse}}$
Sec. 4.1

(a) att-only (b) *w/o* DynamicConv (c) *w/o* C-MLP (d) *w/o* Fusion (e) Mixed Degradation Adaption Block (Full)

Figure A: The illustration of different designs of the proposed MDAB.

single-task models perform competitively, they are slightly outperformed by the all-in-one version in dehazing and deraining. This observation suggests that different degradation types may exhibit shared structures, and that learning them jointly can lead to more generalizable representations.

B.2 Details of the Design for the proposed Mixed Backbone.

To investigate the effectiveness of combining MLP, convolution, and attention mechanisms, we conducted an extensive design-level ablation study. The quantitative results are presented in Tab. 7 of the main manuscript. Here, we provide detailed visual illustrations of each design in Fig. A.

C-MLP. To strengthen channel-wise representation, we introduce a Channel-wise MLP module, denoted as $\text{C-MLP}()$. Given the input feature map $F_{\text{in}}^{\text{mlp}} \in \mathbb{R}^{B\times C\times H\times W}$, we first flatten the spatial dimensions to obtain a sequence $F_{\text{in}}^{\text{mlp}} \in \mathbb{R}^{B\times C\times L}$, where $L = H \times W$. The C-MLP is implemented using two 1D convolutional layers with a GELU activation in between. The GELU function introduces non-linearity, enabling the model to learn more complex and expressive channel-wise transformations. After processing, the output is reshaped back to the original spatial format, yielding $F_{\text{out}}^{\text{mlp}} \in \mathbb{R}^{B\times C\times H\times W}$.

Dynamic Depthwise Convolution. The $\text{DynamicDepthwiseConv}()$ module is designed to capture content-adaptive local structures and is employed in Alg.1 of our main manuscript. As detailed in Alg. A, the input feature $\alpha \in \mathbb{R}^{B\times C\times H\times W}$ is first passed through a global average pooling and two 1×1 convolutions to generate a dynamic depthwise kernel for each channel and sample. The input is reshaped and convolved with the generated kernels using grouped convolution, enabling sample-specific spatial filtering. The resulting output α' maintains the original resolution while embedding adaptive local information.

B.3 Details of the Proposed SPD Contrastive Learning.

As shown in Alg. B, our SPD-based contrastive learning aims to align shallow and latent representations by operating in the space of symmetric positive definite (SPD) matrices. Specifically, given the

Algorithm B SPD Contrastive Learning Optimization Pseudocode

```
# $f_{en}$: encoder
# $f_{de}$: decoder
# $patch\_embedding$: shallow convolutional patch embedding
# $refinement\_conv$: the refinement block and the final convolution
# $spd$: compute SPD feature
for $x$ in loader: # load a minibatch x with n samples

    $F_{\text{shallow}}$ = $patch\_embedding(x)$ # Convolutional Patch Embedding
    $F_{\text{latent}}$ = $f_{en}(F_{\text{shallow}})$

    $\mathbf{C}_s$, $\mathbf{C}_l$= $spd(F_{\text{shallow}})$, $spd(F_{\text{latent}})$ # Comparte SPD (Symmetric Positive Definite) manifold features
    $\mathbf{z}_s$, $\mathbf{z}_l$ = $proj\_norm(\mathbf{C}_s)$, $proj\_norm(\mathbf{C}_l)$ # Projection and normalize

    $F_{\text{recon}}$ = $f_{de}(F_{\text{latent}})$
    $\hat{x}$ = $refinement\_conv(F_{\text{recon}})$

    L = $\mathcal{L}_1(x, \hat{x})$ + $\lambda_{fre} \times \mathcal{L}_{\text{Fourier}}(x, \hat{x})$ + $\lambda_{ctrs} \times \mathcal{L}_{\text{SPD}}(\mathbf{z}_s, \mathbf{z}_l)$ # total loss

    L.backward() # back-propagate
    update($f_{en}$, $f_{de}$, $patch\_embedding$, $refinement\_conv$) # SGD update


def $\mathcal{L}_{\text{Fourier}}$(a, b): # Real-valued Fourier loss
    """
    Refer to Eq.2 of our Supplementary Materails.
    """
    ...
    return loss

def $\mathcal{L}_{\text{SPD}}$(a, b): # Real-valued Fourier loss
    """
    Refer to Eq.5 of our main manuscript.
    """
    ...
    return loss
```

shallow features extracted from the convolutional patch embedding and the latent features produced by the encoder, we compute their second-order channel-wise statistics to obtain SPD representations. These matrices are then vectorized and projected through learnable MLP layers, followed by ℓ_2 normalization to form contrastive embeddings. An InfoNCE-style loss is applied between the shallow and latent embeddings to encourage structural alignment across depth. This contrastive term complements the pixel-level and frequency-based objectives, promoting more discriminative and consistent feature learning without introducing any additional cost during inference. Importantly, by leveraging the geometry of second-order feature statistics, our approach implicitly regularizes the representation space, encouraging intra-instance compactness and inter-degradation separability. This geometrically grounded formulation bridges low-level signal priors with high-level contrastive learning, offering a principled and scalable solution to all-in-one image restoration.

B.4 Ablation Regarding the Optimization Objectives

Tab. C shows that replacing SPD-based contrastive learning with a standard Euclidean-space contrastive loss (*w/o SPD*) results in a clear performance drop, demonstrating the advantage of modeling second-order channel correlations on the SPD manifold rather than relying solely on first-order vector similarities. When the entire contrastive module is removed (*w/o CL & SPD*), performance degrades even further, indicating that aligning shallow and deep features is essential for effective representation learning. Moreover, removing the Fourier loss (*w/o Fourier Loss*) slightly reduces performance, suggesting that frequency-domain supervision provides additional benefits. Overall, the full model achieves the best results, confirming the effectiveness of jointly optimizing spatial, frequency, and SPD-manifold-based structural consistency. Note that throughout all the experiments, we set λ_{ctrs} = 0.05 and λ_{ctrs}=0.1.

Table C: *Ablation Study* of MIRAGE -T on 3 Degradation Setting.

Ablaton	Parms.	Results	
		PSNR (dB, ↑)	SSIM(↓)
w/o CL & SPD	5.80M	32.63 (-0.14)	.916
w/o SPD	6.10M	32.53 (-0.24)	.914
w/o Fourier Loss	5.80M	32.70 (-0.07)	.917
MIRAGE -T *(Full)*	6.21M	32.77	.919

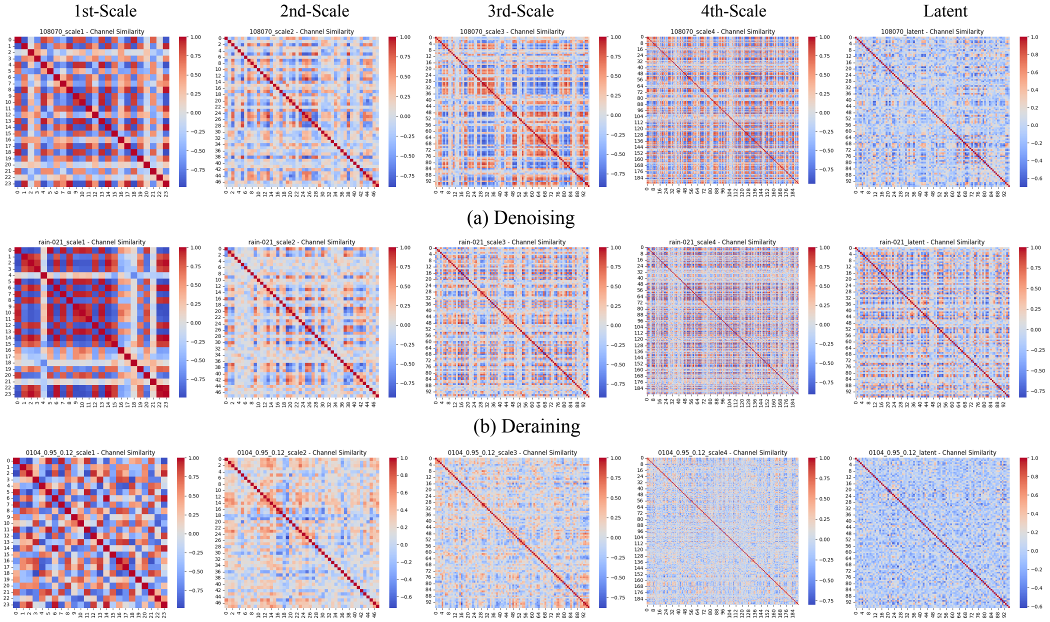

(a) Denoising

(b) Deraining

(b) Dehazing

Figure B: The cross-sclae channel-wise similarity matrix visualization for Denoising, Deraining, and Dehazing.

B.5 Shallow-Latent Feature Similarity

Besides the channel-wise similarity comparison provided in our main manuscript for denoising. We also find consistent findings in other degradation, *i.e.*, raining and hazing. The corresponding channel-wise similarity across scales is provided in Fig. B. These observations reveal several important trends: *(i)* Despite the diversity of degradation types, a consistent pattern emerges across scales. Specifically, from the first to the fourth scale, the overall channel-wise similarity indicates substantial redundancy among feature channels. After channel reduction, the latent features become more decorrelated, which validates the rationale for applying contrastive learning between the latent and shallow (*i.e.*, first-scale) features. *(ii)* Different degradation types exhibit varying degrees of channel redundancy. As illustrated in Fig. B, hazy images tend to produce more inherently independent features, whereas rain-degraded inputs show strong channel-wise redundancy even in the latent space. This suggests that degradations like haze may benefit from larger embedding dimensions to capture more expressive representations, while simpler degradations (*e.g.*, rain) can achieve effective restoration with smaller embedding sizes due to their inherently redundant structure.

These insights open up new directions for adaptive and degradation-aware model design in future research. Notably, this trend is not limited to the three representative samples shown; we observe similar patterns consistently across the dataset in a statistical sense. We plan to conduct a more comprehensive and quantitative investigation of this phenomenon in future work.

C Additional Visual Results.

C.1 3 Degradation

Fig. C presents qualitative comparisons on representative cases of denoising, deraining, and dehazing, benchmarked against recent state-of-the-art methods. The proposed MIRAGE consistently yields more visually faithful restorations, characterized by enhanced structural integrity, finer texture details, and reduced artifacts. These results underscore the effectiveness of our unified framework in handling diverse degradation types while preserving high-frequency information and geometric consistency.

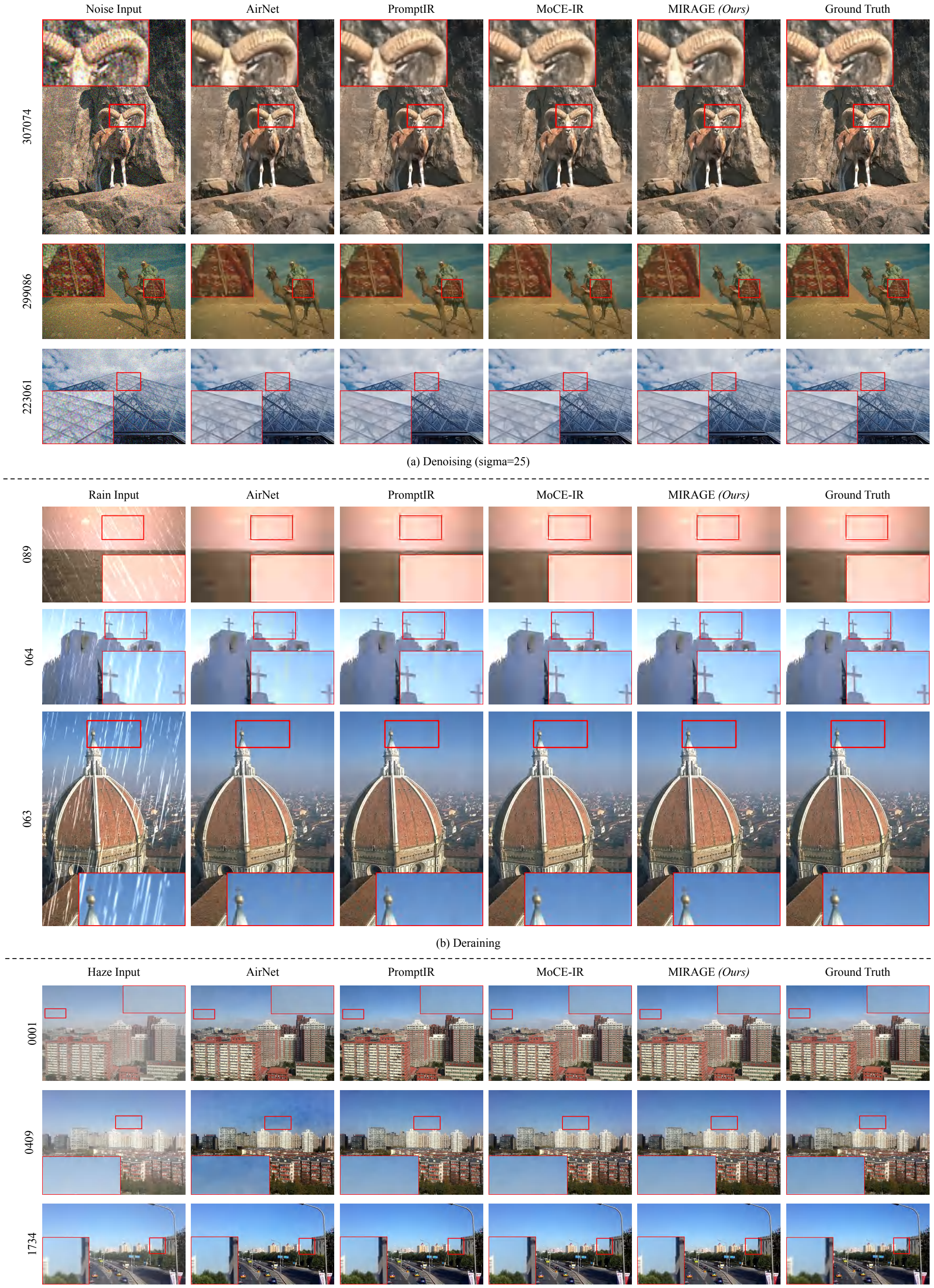

(a) Denoising (sigma=25)

(b) Deraining

Figure C: Visual comparison of MIRAGE with state-of-the-art methods considering three degradations. Zoom in for a better view.

C.2 5 Degradation

For the 5-degradation setting, we provide visual comparisons for the low-light enhancement task in Fig. D. As illustrated, the proposed MIRAGE produces noticeably cleaner outputs with improved luminance restoration and better color consistency compared to MoCE-IR[93], demonstrating its robustness under challenging illumination conditions.

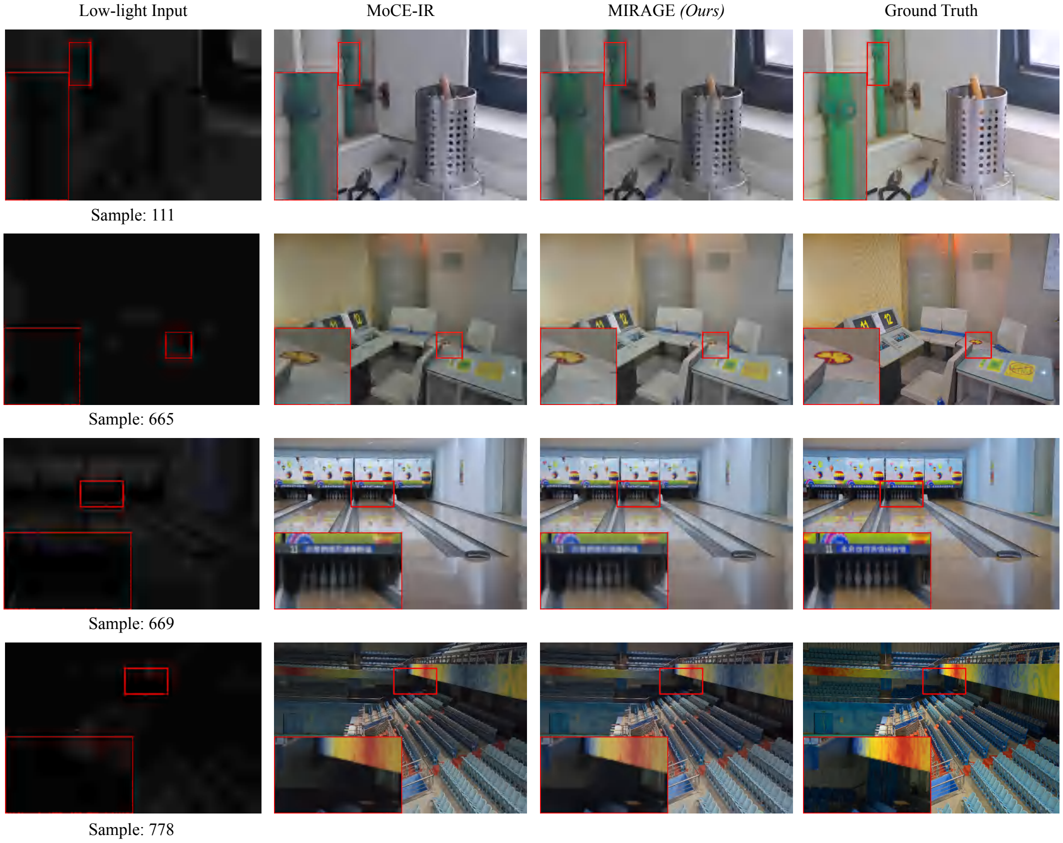

Figure D: Visual comparison of MIRAGE with state-of-the-art methods considering low-light degradation. Zoom in for a better view.

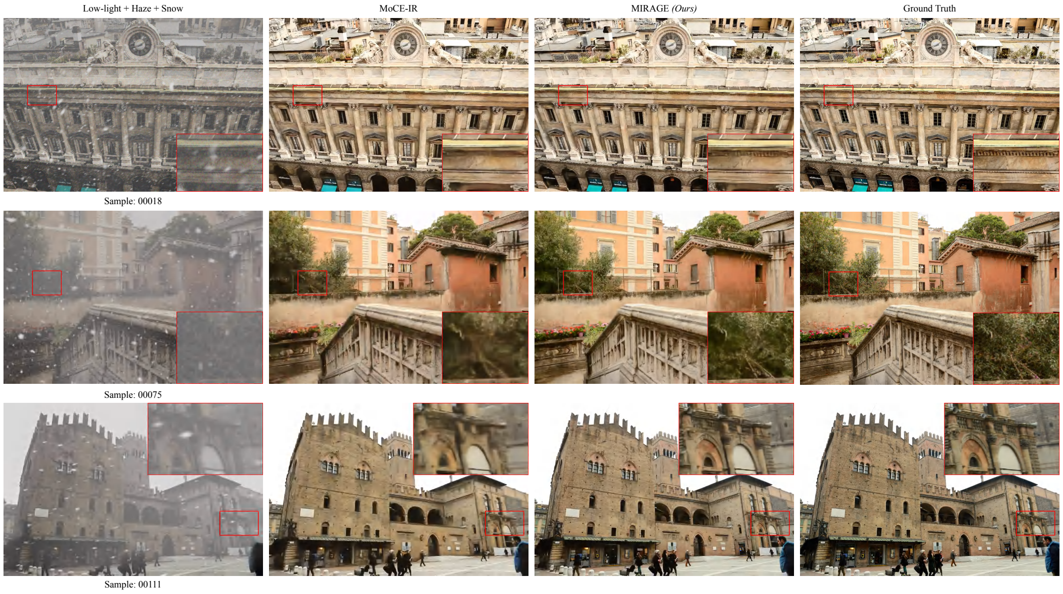

Figure E: Visual comparison of MIRAGE with state-of-the-art methods considering composited degradation (Low-light + Haze + Snow). Zoom in for a better view.

C.3 Composited Degradation

Fig. E and Fig. F present visual comparisons under more challenging composite degradations, namely *low-light* + *haze* + *snow* and *low-light* + *haze* + *rain*, respectively. As observed, our

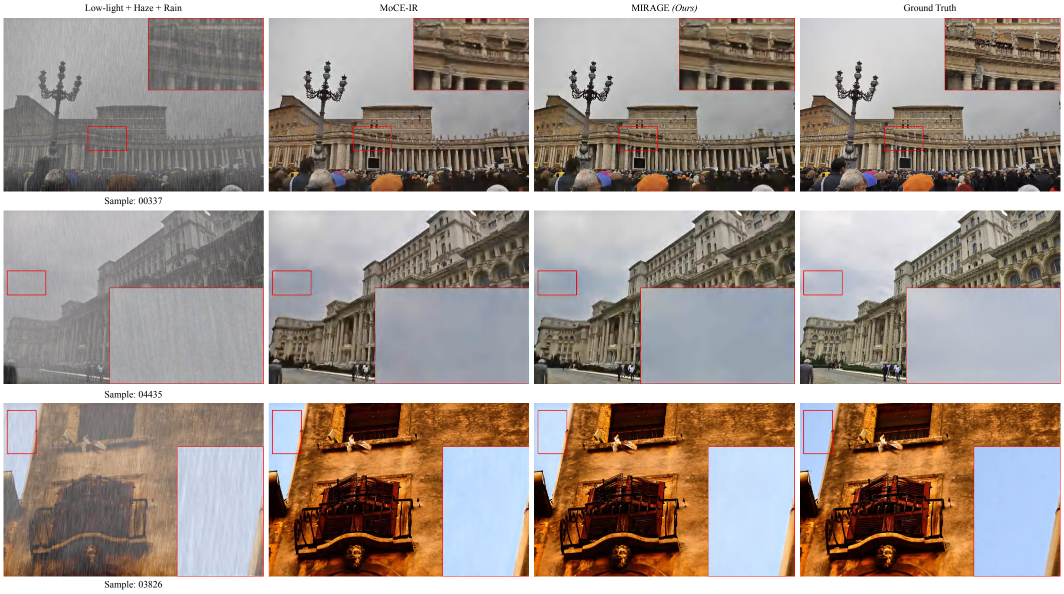

Figure F: Visual comparison of MIRAGE with state-of-the-art methods considering composited degradation (Low-light + Haze + Rain). Zoom in for a better view.

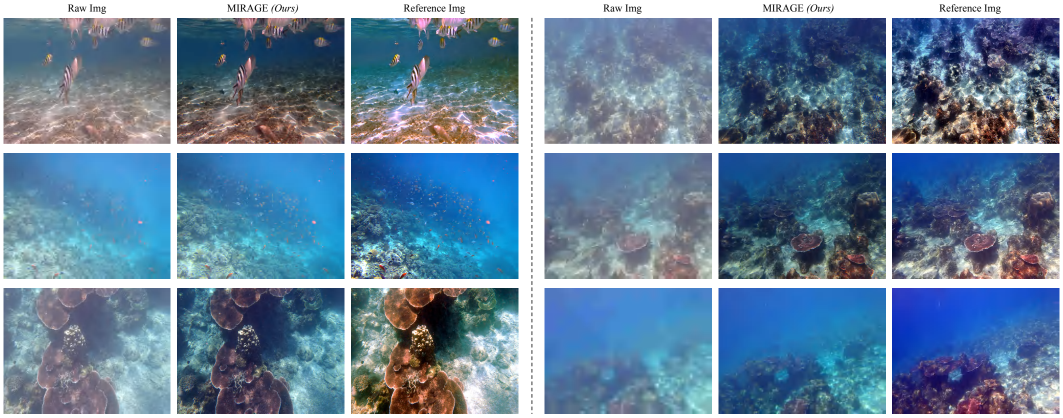

Figure G: Visual results of MIRAGE for Underwater Image Enhancement. Zoom in for a better view.

method reconstructs significantly more scene details and preserves structural consistency, whereas MoCE-IR [93] tends to produce noticeable artifacts and over-smoothed regions under these complex conditions.

C.4 Zero-Shot Underwater Image Enhancement

Fig. G demonstrates that even when directly applied to unseen underwater images, our method is able to effectively enhance visibility and contrast, producing results that are noticeably clearer than the raw input and visually closer to the reference images. This qualitative evidence further validates the strong generalization ability of the proposed framework to unseen domains.

D Limitations and Future Work

While the proposed MIRAGE achieves new state-of-the-art performance on most all-in-one image restoration benchmarks, we observe that its deblurring performance still lags slightly behind MoCE-IR [93]. We attribute this to the relatively compact model size of our current design, which favors efficiency over aggressive capacity. To address this, future work will explore scaling up the model size to be on par with larger architectures such as PromptIR [60], MoCE-IR [93], and AdaIR [11], aiming to further boost performance while maintaining the architectural elegance and efficiency of our design. Moreover, our current SPD-based contrastive learning leverages a conventional InfoNCE loss in Euclidean space after projecting SPD features. While effective, it does not fully exploit the intrinsic geometry of the SPD manifold. As part of future efforts, we plan to investigate geodesic-based contrastive formulations and Riemannian-aware optimization strategies, which may offer a more principled and theoretically grounded way to align structured representations across semantic scales.

E Broader Impact

Image restoration (IR) is a foundational task with widespread applications across photography, remote sensing, surveillance, autonomous driving, medical imaging, and scientific visualization. By proposing a unified and efficient framework capable of handling diverse degradation types with minimal computational cost, our work has the potential to benefit a wide range of real-world scenarios where image quality is compromised due to environmental or hardware constraints. The lightweight design of MIRAGE enables deployment on resource-limited edge devices, such as mobile phones, drones, or embedded cameras in IoT systems. This democratizes access to high-quality image restoration, which may positively impact users in low-resource settings or in critical applications like emergency response and environmental monitoring. From a research perspective, our modular design and SPD-based contrastive formulation may inspire further work on principled representation learning for restoration and beyond, encouraging more geometrically-aware approaches in low-level vision. While our method is intended for general-purpose image enhancement, we acknowledge that improved image restoration techniques can also be misused for deceptive media editing or surveillance applications that raise privacy concerns. We encourage future practitioners to adopt this technology responsibly and in alignment with ethical standards. Our code and models will be released with appropriate licenses and documentation to promote transparency and responsible use.

References

[1] Yuang Ai, Huaibo Huang, Xiaoqiang Zhou, Jiexiang Wang, and Ran He. Multimodal prompt perceiver: Empower adaptiveness, generalizability and fidelity for all-in-one image restoration. In *CVPR*, pages 25432–25444, 2024. 8, 9

[2] Pablo Arbelaez, Michael Maire, Charless Fowlkes, and Jitendra Malik. Contour detection and hierarchical image segmentation. *IEEE TPAMI*, 33(5):898–916, 2010. 1

[3] Mark R Banham and Aggelos K Katsaggelos. Digital image restoration. *IEEE Signal Processing Magazine*, 14(2):24–41, 1997. 3

[4] Tim Brödermann, Christos Sakaridis, Yuqian Fu, and Luc Van Gool. Cafuser: Condition-aware multimodal fusion for robust semantic perception of driving scenes. *IEEE Robotics and Automation Letters*, 2025. 4

[5] Bolun Cai, Xiangmin Xu, Kui Jia, Chunmei Qing, and Dacheng Tao. Dehazenet: An end-to-end system for single image haze removal. *IEEE TIP*, 25(11):5187–5198, 2016. 2

[6] Liangyu Chen, Xiaojie Chu, Xiangyu Zhang, and Jian Sun. Simple baselines for image restoration. In *ECCV*, pages 17–33, 2022. 8

[7] Wei-Ting Chen, Zhi-Kai Huang, Cheng-Che Tsai, Hao-Hsiang Yang, Jian-Jiun Ding, and Sy-Yen Kuo. Learning multiple adverse weather removal via two-stage knowledge learning and multi-contrastive regularization: Toward a unified model. In *IEEE/CVF Conference on Computer Vision and Pattern Recognition (CVPR)*, pages 17632–17641, 2022. 9

[8] Yinbo Chen, Sifei Liu, and Xiaolong Wang. Learning continuous image representation with local implicit image function. In *CVPR*, pages 8628–8638, 2021. 3

[9] Xiaojie Chu, Liangyu Chen, and Wenqing Yu. Nafssr: Stereo image super-resolution using nafnet. In *Proceedings of the IEEE/CVF Conference on Computer Vision and Pattern Recognition (CVPR) Workshops*, pages 1239–1248, June 2022. 9

[10] Marcos V Conde, Gregor Geigle, and Radu Timofte. Instructir: High-quality image restoration following human instructions. In *Proceedings of the European Conference on Computer Vision (ECCV)*, 2024. 7, 8

[11] Yuning Cui, Syed Waqas Zamir, Salman Khan, Alois Knoll, Mubarak Shah, and Fahad Shahbaz Khan. AdaIR: Adaptive all-in-one image restoration via frequency mining and modulation. In *The Thirteenth International Conference on Learning Representations*, 2025. 3, 7, 8, 9, 2

[12] Tri Dao and Albert Gu. Transformers are SSMs: Generalized models and efficient algorithms through structured state space duality. In *International Conference on Machine Learning (ICML)*, 2024. 3

[13] Gridformer: Residual dense transformer with grid structure for image restoration in adverse weather conditions. Gridformer: Residual dense transformer with grid structure for image restoration in adverse weather conditions. *Int. J. Comput. Vis.*, pages 1–23, 2024. 9

[14] Chao Dong, Yubin Deng, Chen Change Loy, and Xiaoou Tang. Compression artifacts reduction by a deep convolutional network. In *ICCV*, pages 576–584, 2015. 3

[15] Yihe Dong, Jean-Baptiste Cordonnier, and Andreas Loukas. Attention is not all you need: Pure attention loses rank doubly exponentially with depth. In *International conference on machine learning*, pages 2793–2803. PMLR, 2021. 2

[16] Yu Dong, Yihao Liu, He Zhang, Shifeng Chen, and Yu Qiao. Fd-gan: Generative adversarial networks with fusion-discriminator for single image dehazing. In *Proceedings of the AAAI conference on artificial intelligence (AAAI)*, 2020. 7, 2

[17] Alexey Dosovitskiy, Lucas Beyer, Alexander Kolesnikov, Dirk Weissenborn, Xiaohua Zhai, Thomas Unterthiner, Mostafa Dehghani, Matthias Minderer, Georg Heigold, Sylvain Gelly, et al. An image is worth 16x16 words: Transformers for image recognition at scale. In *ICLR*, 2020. 2, 3

[18] Huiyu Duan, Xiongkuo Min, Sijing Wu, Wei Shen, and Guangtao Zhai. Uniprocessor: a text-induced unified low-level image processor. In *European Conference on Computer Vision*, pages 180–199. Springer, 2025. 7

[19] Akshay Dudhane, Omkar Thawakar, Syed Waqas Zamir, Salman Khan, Fahad Shahbaz Khan, and Ming-Hsuan Yang. Dynamic pre-training: Towards efficient and scalable all-in-one image restoration. *arXiv preprint arXiv:2404.02154*, 2024. 3

[20] Qingnan Fan, Dongdong Chen, Lu Yuan, Gang Hua, Nenghai Yu, and Baoquan Chen. A general decoupled learning framework for parameterized image operators. *IEEE transactions on pattern analysis and machine intelligence*, 43(1):33–47, 2019. 7, 8

[21] Hongyun Gao, Xin Tao, Xiaoyong Shen, and Jiaya Jia. Dynamic scene deblurring with parameter selective sharing and nested skip connections. In *CVPR*, 2019. 7, 2

[22] Sicheng Gao, Xuhui Liu, Bohan Zeng, Sheng Xu, Yanjing Li, Xiaoyan Luo, Jianzhuang Liu, Xiantong Zhen, and Baochang Zhang. Implicit diffusion models for continuous super-resolution. In *CVPR*, pages 10021–10030, 2023. 3

[23] Albert Gu and Tri Dao. Mamba: Linear-time sequence modeling with selective state spaces. *arXiv preprint arXiv:2312.00752*, 2023. 3

[24] Hang Guo, Jinmin Li, Tao Dai, Zhihao Ouyang, Xudong Ren, and Shu-Tao Xia. Mambair: A simple baseline for image restoration with state-space model. In *ECCV*, 2024. 3, 8

[25] Yu Guo, Yuan Gao, Yuxu Lu, Ryan Wen Liu, and Shengfeng He. Onerestore: A universal restoration framework for composite degradation. In *European Conference on Computer Vision*, 2024. 7, 8, 1

[26] Jia-Bin Huang, Abhishek Singh, and Narendra Ahuja. Single image super-resolution from transformed self-exemplars. In *CVPR*, pages 5197–5206, 2015. 1

[27] Yiping Ji, Hemanth Saratchandran, Peyman Moghaddam, and Simon Lucey. Always skip attention. *arXiv preprint arXiv:2505.01996*, 2025. 2

[28] Hu JiaKui, Zhengjian Yao, Jin Lujia, and Lu Yanye. Universal image restoration pre-training via degradation classification. In *ICLR*, 2025. 1

[29] Kui Jiang, Zhongyuan Wang, Peng Yi, Chen Chen, Baojin Huang, Yimin Luo, Jiayi Ma, and Junjun Jiang. Multi-scale progressive fusion network for single image deraining. In *Proceedings of the IEEE/CVF conference on computer vision and pattern recognition*, pages 8346–8355, 2020. 3, 2

[30] Diederik P Kingma and Jimmy Ba. Adam: A method for stochastic optimization. In *ICLR*, 2015. 1

[31] Lingshun Kong, Jiangxin Dong, Jianjun Ge, Mingqiang Li, and Jinshan Pan. Efficient frequency domain-based transformers for high-quality image deblurring. In *Proceedings of the IEEE/CVF Conference on Computer Vision and Pattern Recognition*, pages 5886–5895, 2023. 3

[32] Wei-Sheng Lai, Jia-Bin Huang, Narendra Ahuja, and Ming-Hsuan Yang. Deep laplacian pyramid networks for fast and accurate super-resolution. In *CVPR*, pages 624–632, 2017. 3

[33] Chen-Yu Lee, Saining Xie, Patrick Gallagher, Zhengyou Zhang, and Zhuowen Tu. Deeply-supervised nets. In *Artificial intelligence and statistics*, pages 562–570. Pmlr, 2015. 2

[34] Boyi Li, Xiulian Peng, Zhangyang Wang, Jizheng Xu, and Dan Feng. Aod-net: All-in-one dehazing network. In *Proceedings of the IEEE international conference on computer vision*, pages 4770–4778, 2017. 2

[35] Boyi Li, Wenqi Ren, Dengpan Fu, Dacheng Tao, Dan Feng, Wenjun Zeng, and Zhangyang Wang. Benchmarking single-image dehazing and beyond. *IEEE Transactions on Image Processing*, 28(1):492–505, 2018. 1

[36] Boyun Li, Xiao Liu, Peng Hu, Zhongqin Wu, Jiancheng Lv, and Xi Peng. All-in-one image restoration for unknown corruption. In *Proceedings of the IEEE/CVF conference on computer vision and pattern recognition*, pages 17452–17462, 2022. 3, 7, 8, 9, 1, 2

[37] Chongyi Li, Chunle Guo, Wenqi Ren, Runmin Cong, Junhui Hou, Sam Kwong, and Dacheng Tao. An underwater image enhancement benchmark dataset and beyond. *IEEE transactions on image processing*, 29:4376–4389, 2019. 1

[38] Ruoteng Li, Loong-Fah Cheong, and Robby T. Tan. Heavy rain image restoration: Integrating physics model and conditional adversarial learning. In *Proceedings of the IEEE Conference on Computer Vision and Pattern Recognition (CVPR)*, pages 1633–1642, 2019. 9

[39] Ruoteng Li, Loong-Fah Cheong, and Robby T Tan. Heavy rain image restoration: Integrating physics model and conditional adversarial learning. In *Proceedings of the IEEE/CVF conference on computer vision and pattern recognition*, pages 1633–1642, 2019. 1

[40] Ruoteng Li, Robby T Tan, and Loong-Fah Cheong. All in one bad weather removal using architectural search. In *IEEE/CVF Conference on Computer Vision and Pattern Recognition (CVPR)*, pages 3175–3185, 2020. 9

[41] Yawei Li, Yuchen Fan, Xiaoyu Xiang, Denis Demandolx, Rakesh Ranjan, Radu Timofte, and Luc Van Gool. Efficient and explicit modelling of image hierarchies for image restoration. In *CVPR*, pages 18278–18289, 2023. 2, 3

[42] Yawei Li, Kai Zhang, Jingyun Liang, Jiezhang Cao, Ce Liu, Rui Gong, Yulun Zhang, Hao Tang, Yun Liu, Denis Demandolx, Rakesh Ranjan, Radu Timofte, and Luc Van Gool. LSDIR: A large scale dataset for image restoration. In *CVPRW*, pages 1775–1787, 2023. 3

[43] Zilong Li, Yiming Lei, Chenglong Ma, Junping Zhang, and Hongming Shan. Prompt-in-prompt learning for universal image restoration. *arXiv preprint arXiv:2312.05038*, 2023. 3

[44] Jingyun Liang, Jiezhang Cao, Guolei Sun, Kai Zhang, Luc Van Gool, and Radu Timofte. SwinIR: Image restoration using Swin transformer. In *ICCVW*, pages 1833–1844, 2021. 3, 8, 9

[45] Bee Lim, Sanghyun Son, Heewon Kim, Seungjun Nah, and Kyoung Mu Lee. Enhanced deep residual networks for single image super-resolution. In *CVPRW*, pages 1132–1140, 2017. 3

[46] Chang Liu, Mengyi Zhao, Bin Ren, Mengyuan Liu, Nicu Sebe, et al. Spatio-temporal graph diffusion for text-driven human motion generation. In *BMVC*, pages 722–729, 2023. 3

[47] Lin Liu, Lingxi Xie, Xiaopeng Zhang, Shanxin Yuan, Xiangyu Chen, Wengang Zhou, Houqiang Li, and Qi Tian. Tape: Task-agnostic prior embedding for image restoration. In *Proceedings of the European Conference on Computer Vision (ECCV)*, 2022. 8

[48] Yun-Fu Liu, Da-Wei Jaw, Shih-Chia Huang, and Jenq-Neng Hwang. Desnownet: Context-aware deep network for snow removal. *IEEE Trans. Image Process.*, 27(6):3064–3073, 2018. 9

[49] Yun-Fu Liu, Da-Wei Jaw, Shih-Chia Huang, and Jenq-Neng Hwang. Desnownet: Context-aware deep network for snow removal. *IEEE Transactions on Image Processing*, 27(6):3064–3073, 2018. 1

[50] Ziwei Luo, Fredrik K Gustafsson, Zheng Zhao, Jens Sjölund, and Thomas B Schön. Image restoration with mean-reverting stochastic differential equations. *arXiv preprint arXiv:2301.11699*, 2023. 3

[51] Ziwei Luo, Fredrik K Gustafsson, Zheng Zhao, Jens Sjölund, and Thomas B Schön. Controlling vision-language models for universal image restoration. In *ICLR*, 2024. 7

[52] Kede Ma, Zhengfang Duanmu, Qingbo Wu, Zhou Wang, Hongwei Yong, Hongliang Li, and Lei Zhang. Waterloo exploration database: New challenges for image quality assessment models. *IEEE TIP*, 26(2):1004–1016, 2016. 1

[53] Qi Ma, Yue Li, Bin Ren, Nicu Sebe, Ender Konukoglu, Theo Gevers, Luc Van Gool, and Danda Pani Paudel. Shapesplat: A large-scale dataset of gaussian splats and their self-supervised pretraining. In *International Conference on 3D Vision 2025*, 2024. 2

[54] David Martin, Charless Fowlkes, Doron Tal, and Jitendra Malik. A database of human segmented natural images and its application to evaluating segmentation algorithms and measuring ecological statistics. In *ICCV*, pages 416–423, 2001. 1

[55] Chong Mou, Qian Wang, and Jian Zhang. Deep generalized unfolding networks for image restoration. In *Proceedings of the IEEE/CVF conference on computer vision and pattern recognition*, pages 17399–17410, 2022. 8

[56] Seungjun Nah, Tae Hyun Kim, and Kyoung Mu Lee. Deep multi-scale convolutional neural network for dynamic scene deblurring. In *CVPR*, pages 3883–3891, 2017. 1

[57] Tam Minh Nguyen, Tan Minh Nguyen, Dung DD Le, Duy Khuong Nguyen, Viet-Anh Tran, Richard Baraniuk, Nhat Ho, and Stanley Osher. Improving transformers with probabilistic attention keys. In *International Conference on Machine Learning*, pages 16595–16621. PMLR, 2022. 4

[58] Tan Nguyen, Tam Nguyen, Hai Do, Khai Nguyen, Vishwanath Saragadam, Minh Pham, Khuong Duy Nguyen, Nhat Ho, and Stanley Osher. Improving transformer with an admixture of attention heads. *Advances in neural information processing systems*, 35:27937–27952, 2022. 4

[59] Ozan Özdenizci and Robert Legenstein. Restoring vision in adverse weather conditions with patch-based denoising diffusion models. *IEEE Trans. Pattern Anal. Mach. Intell.*, 45(8):10346–10357, 2023. 8, 9

[60] Vaishnav Potlapalli, Syed Waqas Zamir, Salman H Khan, and Fahad Shahbaz Khan. Promptir: Prompting for all-in-one image restoration. *Advances in Neural Information Processing Systems*, 36, 2024. 2, 3, 7, 8, 9, 1

[61] Rui Qian, Robby T. Tan, Wenhan Yang, Jiajun Su, and Jiaying Liu. Attentive generative adversarial network for raindrop removal from a single image. In *Proceedings of the IEEE Conference on Computer Vision and Pattern Recognition (CVPR)*, pages 2482–2491, 2018. 9

[62] Rui Qian, Robby T Tan, Wenhan Yang, Jiajun Su, and Jiaying Liu. Attentive generative adversarial network for raindrop removal from a single image. In *Proceedings of the IEEE conference on computer vision and pattern recognition*, pages 2482–2491, 2018. 1

[63] Yanyun Qu, Yizi Chen, Jingying Huang, and Yuan Xie. Enhanced pix2pix dehazing network. In *Proceedings of the IEEE/CVF conference on computer vision and pattern recognition*, pages 8160–8168, 2019. 2

[64] Bin Ren, Yawei Li, Jingyun Liang, Rakesh Ranjan, Mengyuan Liu, Rita Cucchiara, Luc V Gool, Ming-Hsuan Yang, and Nicu Sebe. Sharing key semantics in transformer makes efficient image restoration. *Advances in Neural Information Processing Systems*, 37:7427–7463, 2024. 2

[65] Bin Ren, Yahui Liu, Yue Song, Wei Bi, Rita Cucchiara, Nicu Sebe, and Wei Wang. Masked jigsaw puzzle: A versatile position embedding for vision transformers. In *CVPR*, pages 20382–20391, 2023. 3

[66] Dongwei Ren, Wangmeng Zuo, Qinghua Hu, Pengfei Zhu, and Deyu Meng. Progressive image deraining networks: A better and simpler baseline. In *Proceedings of the IEEE/CVF conference on computer vision and pattern recognition*, pages 3937–3946, 2019. 3

[67] Mengwei Ren, Mauricio Delbracio, Hossein Talebi, Guido Gerig, and Peyman Milanfar. Multiscale structure guided diffusion for image deblurring. In *ICCV*, pages 10721–10733, 2023. 3

[68] Wenqi Ren, Si Liu, Hua Zhang, Jinshan Pan, Xiaochun Cao, and Ming-Hsuan Yang. Single image dehazing via multi-scale convolutional neural networks. In *ECCV*, pages 154–169, 2016. 2

[69] Wenqi Ren, Jinshan Pan, Hua Zhang, Xiaochun Cao, and Ming-Hsuan Yang. Single image dehazing via multi-scale convolutional neural networks with holistic edges. *International Journal of Computer Vision*, 128:240–259, 2020. 3

[70] William Hadley Richardson. Bayesian-based iterative method of image restoration. *Journal of the Optical Society of America*, 62(1):55–59, 1972. 3

[71] Shangquan Sun, Wenqi Ren, Xinwei Gao, Rui Wang, and Xiaochun Cao. Restoring images in adverse weather conditions via histogram transformer. In *European Conference on Computer Vision (ECCV)*, volume 15080, pages 111–129, 2024. 8, 9, 1

[72] Chunwei Tian, Yong Xu, and Wangmeng Zuo. Image denoising using deep cnn with batch renormalization. *Neural Networks*, 2020. 7, 2

[73] Zhengzhong Tu, Hossein Talebi, Han Zhang, Feng Yang, Peyman Milanfar, Alan Bovik, and Yinxiao Li. MAXIM: Multi-axis mlp for image processing. In *CVPR*, pages 5769–5780, 2022. 3

[74] Jeya Maria Jose Valanarasu, Rajeev Yasarla, and Vishal M Patel. TransWeather: Transformer-based restoration of images degraded by adverse weather conditions. In *CVPR*, pages 2353–2363, 2022. 7, 8

[75] Jeya Maria Jose Valanarasu, Rajeev Yasarla, and Vishal M. Patel. Transweather: Transformer-based restoration of images degraded by adverse weather conditions. In *IEEE/CVF Conference on Computer Vision and Pattern Recognition (CVPR)*, pages 2343–2353, 2022. 9, 1

[76] Shashanka Venkataramanan, Amir Ghodrati, Yuki M Asano, Fatih Porikli, and Amirhossein Habibian. Skip-attention: Improving vision transformers by paying less attention. In *ICLR*, 2024. 2, 4

[77] Cong Wang, Jinshan Pan, Wei Wang, Jiangxin Dong, Mengzhu Wang, Yakun Ju, and Junyang Chen. Promptrestorer: A prompting image restoration method with degradation perception. *Advances in Neural Information Processing Systems*, 36:8898–8912, 2023. 3

[78] Huadong Wang, Xin Shen, Mei Tu, Yimeng Zhuang, and Zhiyuan Liu. Improved transformer with multi-head dense collaboration. *IEEE/ACM Transactions on Audio, Speech, and Language Processing*, 30:2754–2767, 2022. 4

[79] Xintao Wang, Ke Yu, Chao Dong, and Chen Change Loy. Recovering realistic texture in image super-resolution by deep spatial feature transform. In *CVPR*, pages 606–615, 2018. 3

[80] Yinhuai Wang, Jiwen Yu, and Jian Zhang. Zero-shot image restoration using denoising diffusion null-space model. *ICLR*, 2023. 3

[81] Chen Wei, Wenjing Wang, Wenhan Yang, and Jiaying Liu. Deep retinex decomposition for low-light enhancement. *arXiv preprint arXiv:1808.04560*, 2018. 1

[82] Wei Wei, Deyu Meng, Qian Zhao, Zongben Xu, and Ying Wu. Semi-supervised transfer learning for image rain removal. In *Proceedings of the IEEE/CVF conference on computer vision and pattern recognition*, pages 3877–3886, 2019. 2

[83] Gang Wu, Junjun Jiang, Kui Jiang, and Xianming Liu. Harmony in diversity: Improving all-in-one image restoration via multi-task collaboration. In *Proceedings of the 32nd ACM International Conference on Multimedia*, pages 6015–6023, 2024. 7, 8

[84] Haiyan Wu, Yanyun Qu, Shaohui Lin, Jian Zhou, Ruizhi Qiao, Zhizhong Zhang, Yuan Xie, and Lizhuang Ma. Contrastive learning for compact single image dehazing. In *Proceedings of the IEEE/CVF conference on computer vision and pattern recognition*, pages 10551–10560, 2021. 3

[85] Da Xiao, Qingye Meng, Shengping Li, and Xingyuan Yuan. Improving transformers with dynamically composable multi-head attention. In *International Conference on Machine Learning*, pages 54300–54318. PMLR, 2024. 4

[86] Chengxing Xie, Xiaoming Zhang, Linze Li, Yuqian Fu, Biao Gong, Tianrui Li, and Kai Zhang. Mat: Multi-range attention transformer for efficient image super-resolution. *IEEE Transactions on Circuits and Systems for Video Technology*, 2025. 3

[87] Fuzhi Yang, Huan Yang, Jianlong Fu, Hongtao Lu, and Baining Guo. Learning texture transformer network for image super-resolution. In *Proceedings of the IEEE/CVF conference on computer vision and pattern recognition*, pages 5791–5800, 2020. 1

[88] Mingde Yao, Ruikang Xu, Yuanshen Guan, Jie Huang, and Zhiwei Xiong. Neural degradation representation learning for all-in-one image restoration. *IEEE Transactions on Image Processing*, 2024. 7

[89] Rajeev Yasarla and Vishal M Patel. Uncertainty guided multi-scale residual learning-using a cycle spinning cnn for single image de-raining. In *Proceedings of the IEEE/CVF conference on computer vision and pattern recognition*, pages 8405–8414, 2019. 2

[90] Tian Ye, Sixiang Chen, Jinbin Bai, Jun Shi, Chenghao Xue, Jingxia Jiang, Junjie Yin, Erkang Chen, and Yun Liu. Adverse weather removal with codebook priors. In *IEEE/CVF International Conference on Computer Vision (ICCV)*, pages 12619–12630, 2023. 9

[91] Tian Ye, Sixiang Chen, Wenhao Chai, Zhaohu Xing, Jing Qin, Ge Lin, and Lei Zhu. Learning diffusion texture priors for image restoration. In *IEEE/CVF Conference on Computer Vision and Pattern Recognition (CVPR)*, pages 2524–2534, 2024. 9

[92] Zongsheng Yue, Jianyi Wang, and Chen Change Loy. ResShift: Efficient diffusion model for image super-resolution by residual shifting. *arXiv preprint arXiv:2307.12348*, 2023. 3

[93] Eduard Zamfir, Zongwei Wu, Nancy Mehta, Yuedong Tan, Danda Pani Paudel, Yulun Zhang, and Radu Timofte. Complexity experts are task-discriminative learners for any image restoration. In *Proceedings of the IEEE/CVF conference on computer vision and pattern recognition*, 2025. 2, 3, 7, 8, 9, 1, 6

[94] Eduard Zamfir, Zongwei Wu, Nancy Mehta, Yulun Zhang, and Radu Timofte. See more details: Efficient image super-resolution by experts mining. In *International Conference on Machine Learning*. PMLR, 2024. 3

[95] Syed Waqas Zamir, Aditya Arora, Salman Khan, Munawar Hayat, Fahad Shahbaz Khan, and Ming-Hsuan Yang. Restormer: Efficient transformer for high-resolution image restoration. In *CVPR*, pages 5728–5739, 2022. 2, 3, 8, 9

[96] Syed Waqas Zamir, Aditya Arora, Salman Khan, Munawar Hayat, Fahad Shahbaz Khan, Ming-Hsuan Yang, and Ling Shao. Multi-stage progressive image restoration. In *CVPR*, pages 14821–14831, 2021. 7

[97] Haijin Zeng, Xiangming Wang, Yongyong Chen, Jingyong Su, and Jie Liu. Vision-language gradient descent-driven all-in-one deep unfolding networks. In *Proceedings of the IEEE/CVF conference on computer vision and pattern recognition*, 2025. 3, 7, 8

[98] He Zhang and Vishal M Patel. Density-aware single image de-raining using a multi-stream dense network. In *Proceedings of the IEEE conference on computer vision and pattern recognition*, pages 695–704, 2018. 2

[99] Jinghao Zhang, Jie Huang, Mingde Yao, Zizheng Yang, Hu Yu, Man Zhou, and Feng Zhao. Ingredient-oriented multi-degradation learning for image restoration. In *Proceedings of the IEEE/CVF Conference on Computer Vision and Pattern Recognition*, pages 5825–5835, 2023. 3, 7, 8, 9

[100] Kai Zhang, Wangmeng Zuo, Yunjin Chen, Deyu Meng, and Lei Zhang. Beyond a gaussian denoiser: Residual learning of deep cnn for image denoising. *IEEE TIP*, 26(7):3142–3155, 2017. 3, 2

[101] Kai Zhang, Wangmeng Zuo, Shuhang Gu, and Lei Zhang. Learning deep cnn denoiser prior for image restoration. In *CVPR*, pages 3929–3938, 2017. 3, 2

[102] Kai Zhang, Wangmeng Zuo, and Lei Zhang. FFDNet: Toward a fast and flexible solution for cnn-based image denoising. *IEEE TIP*, 27(9):4608–4622, 2018. 2

[103] Leheng Zhang, Yawei Li, Xingyu Zhou, Xiaorui Zhao, and Shuhang Gu. Transcending the limit of local window: Advanced super-resolution transformer with adaptive token dictionary. *arXiv preprint arXiv:2401.08209*, 2024. 3

[104] Yulun Zhang, Kunpeng Li, Kai Li, Bineng Zhong, and Yun Fu. Residual non-local attention networks for image restoration. *arXiv preprint arXiv:1903.10082*, 2019. 3

[105] Mengyi Zhao, Mengyuan Liu, Bin Ren, Shuling Dai, and Nicu Sebe. Denoising diffusion probabilistic models for action-conditioned 3d motion generation. In *ICASSP 2024-2024 IEEE International Conference on Acoustics, Speech and Signal Processing (ICASSP)*, pages 4225–4229. IEEE, 2024. 3

[106] Xu Zheng, Yuanhuiyi Lyu, and Lin Wang. Learning modality-agnostic representation for semantic segmentation from any modalities. In *European Conference on Computer Vision*, pages 146–165. Springer, 2024. 3

[107] Jinjing Zhu, Yunhao Luo, Xu Zheng, Hao Wang, and Lin Wang. A good student is cooperative and reliable: Cnn-transformer collaborative learning for semantic segmentation. In *Proceedings of the IEEE/CVF International Conference on Computer Vision*, pages 11720–11730, 2023. 2

[108] Lianghui Zhu, Bencheng Liao, Qian Zhang, Xinlong Wang, Wenyu Liu, and Xinggang Wang. Vision mamba: Efficient visual representation learning with bidirectional state space model. *arXiv preprint arXiv:2401.09417*, 2024. 3

[109] Yurui Zhu, Tianyu Wang, Xueyang Fu, Xuanyu Yang, Xin Guo, Jifeng Dai, Yu Qiao, and Xiaowei Hu. Learning weather-general and weather-specific features for image restoration under multiple adverse weather conditions. In *IEEE/CVF Conference on Computer Vision and Pattern Recognition (CVPR)*, pages 21747–21758, 2023. 8, 9, 1

[110] Yurui Zhu, Tianyu Wang, Xueyang Fu, Xuanyu Yang, Xin Guo, Jifeng Dai, Yu Qiao, and Xiaowei Hu. Learning weather-general and weather-specific features for image restoration under multiple adverse weather conditions. In *Proceedings of the IEEE/CVF conference on computer vision and pattern recognition*, pages 21747–21758, 2023. 7